Available online at www.sciencedirect.com
ScienceDirect
Comput. Methods Appl. Mech. Engrg. 305 (2016) 37–61
Computer methods in applied mechanics and engineering
www.elsevier.com/locate/cma

Parallel hierarchical multiscale modelling of hydro-mechanical problems for saturated granular soils

Ning Guo*, Jidong Zhao

Department of Civil and Environmental Engineering, The Hong Kong University of Science and Technology, Clearwater Bay, Kowloon, Hong Kong

Received 23 August 2015; received in revised form 29 February 2016; accepted 3 March 2016
Available online 10 March 2016

Abstract

This paper extends the hierarchical multiscale approach developed earlier by the authors to model the coupled hydro-mechanical behaviour for saturated granular soils. Based on a hierarchical coupling of the finite element method (FEM) and the discrete element method (DEM), the approach employs the FEM to solve a boundary value problem while using the DEM to derive the required nonlinear material responses at each FEM Gauss integration point. It helps to bypass the phenomenological constitutive model required in the conventional FEM simulations and offers a natural pathway for scale bridging. The current extension features further key consideration of the coupled hydro-mechanical behaviour in a saturated granular soil due to the presence of pore fluid and its flow. By invoking Terzaghi's effective stress principle, a **u**–p formulation is proposed for the multiscale framework to derive the effective stress from DEM solution of the representative volume element (RVE) embedded at each Gauss point which is then superimposed with the pore fluid pressure to obtain the total stress in solving the coupled governing equations for a fluid–solid mixture. This extension greatly enriches the predictive capacity of the multiscale approach for simulating saturated granular soils relevant to a wide variety of important civil/mining applications. The new approach is first benchmarked by closed-form solutions to classical 1D and 2D consolidation problems. It is then applied to simulate globally undrained biaxial compression tests on both dense and loose soils subjected to large deformation. We further discuss interesting fluid flow patterns and the failure modes (both localisation and diffuse liquefaction) observed from the simulations and provide detailed cross-scale analyses.

Keywords: Hierarchical multiscale modelling; Parallel computing; Coupled hydro-mechanical problem; Saturated granular soil; Strain localisation; Diffuse liquefaction

1. Introduction

Fluid–solid interactions in saturated granular soils underpin the operation and safety management for key infrastructures in civil, mining and reservoir engineering. Many catastrophic geohazards, from dam/embankment failure and debris flow to submarine landslides and earthquake liquefaction, are attributable to the presence of pore

* Corresponding author. Fax: +852 23581534.
E-mail address: ceguo@connect.ust.hk (N. Guo).

http://dx.doi.org/10.1016/j.cma.2016.03.004
0045-7825/

fluids and their interactions with soil particles. A thorough understanding of the underlying dominant mechanisms is vital for hazard mitigations and may as well provide useful references for economic and safe design for many other engineering and industrial branches.

There are two broad categories of numerical approaches in simulating fluid-saturated solids. The first class treats the fluid–solid mixture as a continuum, and employs numerical schemes such as the seminal $\mathbf{u}$–p formulation [1] to solve the governing equations of a hydro-mechanical system (where $\mathbf{u}$ stands for the displacement of the solid phase and p is the pore fluid pressure). In recent years, there has emerged a second class of micromechanics-based methods, where the solid phase is modelled as a collection of discrete particles based typically on the discrete element method (DEM), while the fluid phase is still treated as a continuum or semi-continuum and is solved by the computational fluid dynamics (CFD) method or the lattice Boltzmann method (LBM). The micromechanics-based approaches are advantageous in providing direct microscopic insights into the fluid–solid interactions and facilitating a cross-scale understanding of the behaviours of the mixture [2–7]. They however may suffer major drawbacks including prohibitive computational cost, requiring for intricate treatment of moving boundaries between fluid and solids (e.g., the evolving pore morphology in a granular material is notoriously difficult to characterise and model) as well as over-simplified and most often empirically based interaction laws. The continuum-based approaches on the other hand, when used in conjunction with the finite element method (FEM), have indeed been proven robust and efficient in dealing with a broad frequency range, from quasi-static to seismic loading conditions, and have been prevailing in solving a wide variety of boundary value problems (BVPs) of practical importance (see Ref. [1] and references therein). Some issues related to their use in conventional FEM, including mesh distortion and sensitivity, have also been addressed recently by meshless methods, such as the element-free Galerkin, smoothed particle hydrodynamics, reproducing kernel particle and material point methods [8–11]. Notwithstanding of their success, conventional continuum approaches commonly need presumed constitutive models to describe the material response. For example, many continuum-based studies today are still following the simple linear elasticity model proposed by Biot [12] in coupled analysis of a hydro-mechanical system. It however has long been proved to be too oversimplified to adequately describe the complicated shear behaviour of granular soils, exemplified by state/loading path dependency, anisotropy, non-coaxiality and cyclic hysteresis, among others. Various advanced plasticity models have been developed and have become the mainstream in modelling the behaviour of saturated granular soils. Compared to Biot's elasticity, these models indeed provide greatly improved predictive performance on soil behaviours, but have to pay the price of introducing a large number of model parameters in their model formulations and many of them are phenomenological in nature.

The present study aims to develop a relatively new methodology to model the behaviour of fluid-saturated granular soils, by combining the advantages of both classes of approaches mentioned above while mitigating their pitfalls. In particular, we wish to utilise the robustness and efficiency of continuum approaches in tackling practical BVPs, and meanwhile attempt to gain cross-scale insights with effective linking of macro and micro scales of soils. In this regard, the hierarchical multiscale approach recently developed by the authors and other researchers [13–23] may offer a viable option. In this multiscale approach, the FEM is used to discretise the problem domain and to solve the governing equations by virtue of its efficiency in solving large-scale BVPs; meanwhile DEM packings are embedded in the Gauss points of the FEM mesh, serving as representative volume elements (RVEs) to derive the local material constitutive responses. The hierarchical coupling of FEM and DEM naturally helps to avoid the needs for developing constitutive models and fitting their phenomenological model parameters. Meanwhile the embedded DEM simulations enable the typical characteristics of soil behaviour to be effectively captured and reproduced. By combining the continuum mechanics and the micromechanics, the hierarchical approach also facilitates straightforward cross-scale analyses of granular soils. Demonstrated examples have been showcased in the aforementioned works. However, the hierarchical multiscale approach so far has been developed to model dry granular soils. The soil responses simulated by the approach can at best be interpreted as drained behaviours only. Capturing the full behaviour of a fluid-saturated granular soil proves to be more important for many practical applications, regardless it is under drained, undrained or partially drained conditions. Therefore in this study, we attempt to extend our original hierarchical multiscale approach to address the coupled hydro-mechanical problems for saturated granular soils.

Since DEM constitutes a key component in the hierarchical multiscale approach, it may appear to be straightforward to consider the fluid–solid interaction directly at the micro level of the framework, i.e. to simulate the interaction of pore fluid and soil particles directly within the DEM packing and to derive the *total stress* from the local RVE simulation for the global FEM solution. There are indeed advanced tools already being developed in the literature for such purposes, e.g., the coupled CFD/DEM approach [2–4] and the coupled LBM/DEM approach [5–7].

However, these methods are known to be computationally expensive for single-RVE calculation already, and may quickly fail to work for a practical problem involving hundreds to thousands of RVE packings. To make it worse, the internal structure within a granular material evolves constantly with the loading, and so are the pore morphology and pore fluid flow, which poses tremendous technical and computational challenges to these methods too. In view of these difficulties, a computationally more economic way is proposed by using the **u**–p formulation as mentioned before in conjunction with the Terzaghi's effective stress principle [24]. The fluid flow can then be solved by the balance of mass equation in the macro scale. Moreover, numerical issues such as convergence and stabilisation pertaining to solving the governing **u**–p equations have been well resolved [25–27] and can be used in the multiscale modelling. The strategy is rather similar to the conventional coupled FEM, except that the *effective stress* is derived directly from the embedded DEM simulation at each Gauss point instead of being based on the presumed constitutive model. While the primary goal here is to model granular soils in saturated condition, the proposed strategy for coupled hierarchical multiscale modelling can indeed be easily adapted for simulating unsaturated granular soils as well, e.g., by considering proper capillary force in the DEM part based on the liquid-bridge model [28]. In this latter case, the RVE simulation helps to derive the *Bishop's effective stress* in unsaturated conditions.

While the concept described above is easy to understand, there remains issues to be considered pertaining to the solution scheme of the coupled **u**–p formulation and the parallel computing of the hierarchical multiscale approach. In solving the governing equations for a coupled system based on the **u**–p formulation, there are two options which can yield converged, accurate solutions. One is referred to as the fully coupled scheme, where a full matrix for the coupled system is assembled and the unknowns for solid displacement and pore fluid pressure are solved simultaneously [29,30]. The other is the iteratively coupled scheme [10,31–33]. In the latter scheme, the entire system is partitioned and treated by two sequential solvers—a mechanical solver for solid displacement and a fluid solver for pore pressure. Gauss–Seidel-like iterations are then implemented to find the converged solution of the two primary unknowns. Since the first scheme may lead to ill-conditioned stiffness matrix, the second scheme is adopted in the study. Indeed, as will be shown, the sequential iterative scheme suits well the coupled hierarchical multiscale approach due to its flexibility and modularity, since our previous work for the dry case [13–17] can be directly adapted as the mechanical solver with minor modifications in the scheme. Parallelisation is another concern since a practical problem may need tens of thousands of RVEs and the DEM computation of each of them is considerably time consuming. The increase in computing time may amount to magnitude higher when the iterative procedure applies. Fortunately, these DEM simulations are independent with one another within the hierarchical multiscale approach, which renders parallelisation easily achievable. The rapid development of multi-core and distributed computing technology will further facilitate the application of the approach for large-scale coupled problems.

The rest of the paper is organised as follows. In Section 2, the governing equations and the FEM discretisation are presented first, followed by the formulation and solution procedure of the coupled hierarchical multiscale approach. Section 3 presents benchmarks of the implemented approach by solving classical 1D and 2D consolidation problems on an elastic soil. In Section 4, the multiscale approach is further applied to investigate the globally undrained biaxial compression tests on dense and loose soils. Major conclusions are summarised in Section 5. In the presentation, we follow the indicial notation, comma derivative and Einstein summation convention for vectors and tensors, and use boldface letters for matrices.

2. Approach and formulation

2.1. Governing equations

The **u**–p formulation proposed in Ref. [1] involves two primary unknowns in the governing equations for a saturated granular soil: one is the displacement vector **u** of the solid skeleton; the other is the pore fluid pressure p of the fluid phase. The momentum equilibrium of the fluid–solid mixture in the quasi-static limit writes:

$$\sigma_{ij,j} + \rho\, b_i = 0 \tag{1}$$

where σ_{ij} is the total stress tensor, ρ is the bulk density of the mixture, and b_i is the unit body force due to gravity. According to the Terzaghi's effective stress principle, the total stress σ_{ij} is a superposition of the effective stress σ'_{ij} carried by the soil skeleton (transmitted through interparticle contacts) and the pore fluid pressure sustained by the

pore fluid, via

$$\sigma_{ij} = \sigma'_{ij} - \alpha\, p\, \delta_{ij} \tag{2}$$

where δ_{ij} is the Kronecker delta, and α is the Biot coefficient which is approximately equal to 1 for a granular soil.

The governing equation of mass conservation for the fluid phase writes

$$[k_{ij}(-p_{,j} + \rho_f\, b_j)]_{,i} + \alpha\, \dot{u}_{i,i} + \frac{n}{K_f}\dot{p} = 0 \tag{3}$$

where ρ_f is the density of the fluid. k_{ij} is the permeability tensor (in the unit of $\mathrm{m}^2/(\mathrm{Pa\,s})$). The hydraulic conductivity (in the unit of m/s) can be obtained by multiplying k_{ij} with the specific weight of the fluid. $k_{ij}(-p_{,j} + \rho_f\, b_j)$ $(= v_i)$ gives the Darcy flux. $u_{i,i}$ is the volumetric stretch of the solid skeleton, n is the porosity of the mixture, and K_f is the bulk modulus of the fluid. A superimposed dot symbol indicates time derivative of the variable. In Eq. (3), the solid grain is assumed totally incompressible.

Eqs. (1) and (3) constitute the governing equations for the hydro-mechanical system to be considered in the study. The coupling manifests itself in that the pore fluid pressure is present in the momentum equilibrium equation to affect the solid displacement, while the latter influences the mass balance of the fluid through volumetric change. It is also noted that the porosity n and the permeability k_{ij} in Eq. (3) may also change due to the deformation of the solid phase. While anisotropy may present in practical cases, the present study treats the permeability of the material as isotropic for simplicity, i.e. $k_{ij} = k\,\delta_{ij}$, where the scalar permeability k is estimated from the empirical Kozeny–Carman equation for a packing of spherical particles [34,35]

$$k = \frac{\bar{d}^2\, n^3}{180\, \mu_f\, (1-n)^2} \tag{4}$$

where $\bar{d}$ is the average diameter of the soil grain, and μ_f is the dynamic viscosity of the fluid.

The complete boundary conditions for the system are

$$\sigma_{ij}\, n_j = \bar{t}_i \quad \text{on } \Gamma_t \tag{5}$$

$$u_i = \bar{u}_i \quad \text{on } \Gamma_u \tag{6}$$

$$p = \bar{p} \quad \text{on } \Gamma_p \tag{7}$$

$$-v_i\, n_i = \bar{q} \quad \text{on } \Gamma_q \tag{8}$$

where n_i is the outward normal of the boundary of the problem domain; $\bar{t}_i$, $\bar{u}_i$, $\bar{p}$ and $\bar{q}$ are the prescribed boundary traction on Γ_t, solid displacement on Γ_u, pore fluid pressure on Γ_p and fluid influx on Γ_q, respectively. Besides the governing equations and the prescribed boundary and initial conditions, a constitutive relation describing the effective stress–strain behaviour of the soil skeleton is needed by FEM to solve the BVP. In conventional continuum modelling, a phenomenologically based constitutive model is commonly assumed, which can be bypassed in the current hierarchical multiscale approach. Instead, separate discrete RVE packings will be assigned to the Gauss points of the FEM mesh to derive the local material responses by DEM computations. The details will be discussed in Section 2.3.

2.2. Discretisation

The global governing equations of the coupled hydro-mechanical problem are solved by an open-source FEM code `Escript` [36]. In the FEM, spatial discretisations of the displacement field $\mathbf{u}(\mathbf{x}, t)$ and the pore fluid pressure $p(\mathbf{x}, t)$ are written as

$$\mathbf{u}(\mathbf{x}, t) \approx \mathbf{u}^h(\mathbf{x}, t) = \sum_{I \in \mathcal{N}_u} \mathbf{N}_{uI}(\mathbf{x})\mathbf{u}_I(t) \tag{9}$$

$$p(\mathbf{x}, t) \approx p^h(\mathbf{x}, t) = \sum_{I \in \mathcal{N}_p} \mathbf{N}_{pI}(\mathbf{x})\mathbf{p}_I(t) \tag{10}$$

where $\mathcal{N}_u$ and $\mathcal{N}_p$ are the sets of the displacement and the pressure nodes, respectively; $\mathbf{N}_u$ and $\mathbf{N}_p$ are the shape functions for the displacement and the pressure fields, respectively. To satisfy the Ladyzhenskaya–Babuska–Brezzi

condition [37] in dealing with nearly incompressible fluids inside solids with low permeability, a higher order is commonly adopted for the interpolation function of $\mathbf{N}_u$ than that for $\mathbf{N}_p$ to avoid oscillations in the solutions. The derivation of the weak form of Eqs. (1) and (3) follows the standard FEM procedure. To avoid distraction, we only present the discretisation of the momentum equilibrium equation and elaborate the implementation of the hierarchical multiscale approach in Section 2.3.

For the time integration, a generalised midpoint rule is adopted

$$\mathbf{u}^{(n+\theta)} = (1-\theta)\,\mathbf{u}^{(n)} + \theta\,\mathbf{u}^{(n+1)} \tag{11}$$

$$\dot{\mathbf{u}}^{(n+\theta)} = (\mathbf{u}^{(n+1)} - \mathbf{u}^{(n)})/\Delta t \tag{12}$$

$$p^{(n+\theta)} = (1-\theta)\,p^{(n)} + \theta\,p^{(n+1)} \tag{13}$$

$$\dot{p}^{(n+\theta)} = (p^{(n+1)} - p^{(n)})/\Delta t \tag{14}$$

where the superscripts (n) and $(n+1)$ denote two consecutive loading steps; Δt $(=t^{(n+1)} - t^{(n)})$ is the time step increment; θ is a value between 0 and 1. The scheme is explicit when $\theta = 0$ and implicit otherwise. In the study, we set $\theta = 1$ which provides unconditional stability in the adopted iterative coupling method, as to be discussed in Section 2.4.1.

2.3. Hierarchical multiscale approach

The hierarchical multiscale approach has been presented in Refs. [13–17] and will be employed as the mechanical solver in the current study. For the sake of completeness, the method is briefly summarised in the following.

2.3.1. FEM solver

To obtain the variational form, we multiply Eq. (1) by a test function δu_i, integrate over the problem domain Ω and apply the Gaussian theorem

$$\int_\Omega \delta u_{i,j}\,\sigma'_{ij}\,d\Omega - \int_\Omega \delta u_{i,i}\,\alpha\,p\,d\Omega - \int_\Omega \delta u_i\,\rho\,b_i\,d\Omega = \int_{\Gamma_t} \delta u_i\,\bar{t}_i\,d\Gamma_t. \tag{15}$$

Using Eqs. (9) and (10), the above equation can be written in the following semi-discrete form

$$\int_\Omega \delta\mathbf{u}^{\mathrm{T}}(\mathbf{B}^{\mathrm{T}}\boldsymbol{\sigma}'^{(0)} + \mathbf{B}^{\mathrm{T}}\mathbf{C}\mathbf{B}\Delta\mathbf{u})d\Omega - \int_\Omega \alpha\,\delta\mathbf{u}^{\mathrm{T}}(\mathbf{B}^{\mathrm{T}}\mathbf{m}\mathbf{N}_p\,\mathbf{p})d\Omega$$
$$- \int_\Omega \rho\,\delta\mathbf{u}^{\mathrm{T}}(\mathbf{N}_u^{\mathrm{T}}\,\mathbf{b})d\Omega = \int_{\Gamma_t} \delta\mathbf{u}^{\mathrm{T}}(\mathbf{N}_u^{\mathrm{T}}\,\bar{\mathbf{t}})d\Gamma_t \tag{16}$$

where $\mathbf{B}$ is the strain–displacement matrix, $\boldsymbol{\sigma}'^{(0)}$ is the current (old) effective stress, and $\mathbf{C}$ is the tangent operator which is homogenised from the DEM packing. $\Delta\mathbf{u}$ is the unknown nodal displacement increment. $\mathbf{m}$ $(=(1,1,0)^{\mathrm{T}}$ in 2D) is the Dirac delta function. Note that in conventional continuum-based constitutive modelling approach, Jaumann rate of stress tensor is commonly used for the stress update for objectiveness in large deformation problems involving rigid body rotations. However, in the current multiscale approach, $\boldsymbol{\sigma}'$ will be directly homogenised from the RVE packing for each update (see Eq. (21)). The homogenised stress tensor can fully reflect the rigid body rotations of the RVE packing and remains objective for each update. Hence, Jaumann rate is not needed for stress update in the current multiscale study.

After eliminating $\delta\mathbf{u}^{\mathrm{T}}$ at both sides of Eq. (16) and defining the following global stiffness matrix

$$\mathbf{K} = \int_\Omega \mathbf{B}^{\mathrm{T}}\mathbf{C}\mathbf{B}\,d\Omega, \tag{17}$$

the compact equation system in matrix form for $\Delta\mathbf{u}$ can be obtained

$$\mathbf{K}\,\Delta\mathbf{u} = \mathbf{R} \tag{18}$$

where the right-hand side term $\mathbf{R}$ is the residual force which is contributed by several terms as seen from Eq. (16)

$$\mathbf{R} = \int_{\Omega} \rho\, \mathbf{N}_u^{\mathrm{T}}\, \mathbf{b}\, d\Omega + \int_{\Omega} \alpha\, \mathbf{B}^{\mathrm{T}} \mathbf{m}\, \mathbf{N}_p\, \mathbf{p}\, d\Omega + \int_{\Gamma_t} \mathbf{N}_u^{\mathrm{T}}\, \bar{\mathbf{t}}\, d\Gamma_t - \int_{\Omega} \mathbf{B}^{\mathrm{T}} \boldsymbol{\sigma}'^{(0)}\, d\Omega. \tag{19}$$

Compared with our previous work [13–17], Eq. (19) contains an extra term accounting for the pore fluid pressure in the residual force vector (the second term on the right-hand side).

For a general nonlinear problem, Eq. (18) is solved by means of the Newton–Raphson method, where $\mathbf{K}$ and $\mathbf{R}$ are updated through iterations with changes of the tangent operator and the effective stress at the local material points. Both quantities are homogenised from the discrete packings and are updated by the local DEM solver. A converged solution is found when the residual $\mathbf{R}$ is smaller than a prescribed tolerance

$$\frac{\|\mathbf{R}\|_2}{\|\mathbf{R}_0\|_2} \leq \mathrm{TOL}_f \tag{20}$$

where $\| \bullet \|_2$ denotes the L^2 norm of the quantity, $\mathbf{R}_0$ is the initial residual force at the beginning of each loading step.

2.3.2. DEM solver

In the hierarchical multiscale approach, we embed a DEM assembly as the RVE at every Gauss point of the FEM mesh to derive the local constitutive response of the material. The boundary condition for the local RVE is prescribed according to the FEM nodal displacement $\mathbf{u}$ (via interpolation). During each Newton–Raphson iteration, the RVE packing is deformed according to the interpolated displacement gradient $u_{i,j}$ at the corresponding Gauss point which contains both the strain ε_{ij} $(=(u_{i,j} + u_{j,i})/2)$ and the rigid body rotation ω_{ij} $(=u_{i,j} - \varepsilon_{ij})$. Once an equilibrium solution for the deformed packing is achieved, the DEM returns the updated effective stress and the tangent operator to the FEM. The updated σ'_{ij} will be used in Eq. (19) to evaluate the residual; and the new C_{ijkl} will be used to update the stiffness matrix $\mathbf{K}$ using Eq. (17). The effective stress tensor is homogenised from the RVE packing using the Love's formula

$$\sigma'_{ij} = \frac{1}{V} \sum_{N^c} d_i^c\, f_j^c \tag{21}$$

where V is the volume of the RVE packing, N^c is the number of contacts inside the volume, and f_i^c and d_i^c are the contact force and the branch vector connecting the centres of the two contacting particles, respectively. An interparticle contact is illustrated in Fig. 1. Since the stress defined in Eq. (21) is contributed by the interparticle contacts, it exactly measures the *effective stress* in Eq. (2) as envisaged by Terzaghi. Two common scalar stress measurements—the mean effective stress σ'_v and the deviatoric stress σ_d are calculated (in 2D)

$$\sigma'_v = \frac{1}{2}\sigma'_{ii} \tag{22}$$

$$\sigma_d = \sqrt{\frac{1}{2} s_{ij} s_{ij}} \tag{23}$$

where s_{ij} $(=\sigma'_{ij} - \sigma'_v\, \delta_{ij})$ is the deviatoric stress tensor. Note that we have followed the convention in solid mechanics to treat extension as positive. Similarly, two common scalar strain measurements—the volumetric strain ε_v and the deviatoric strain ε_d are also defined from the local strain tensor (in 2D)

$$\varepsilon_v = \varepsilon_{ii} \tag{24}$$

$$\varepsilon_d = \sqrt{2\, e_{ij} e_{ij}} \tag{25}$$

where e_{ij} $(=\varepsilon_{ij} - \varepsilon_v\, \delta_{ij}/2)$ is the deviatoric strain tensor.

The tangent operator C_{ijkl} of a RVE packing is homogenised based on the assumption of uniform deformation [38,39]

$$C_{ijkl} = \frac{1}{V} \sum_{N^c} (k_n\, n_i^c\, d_j^c\, n_k^c\, d_l^c + k_t\, t_i^c\, d_j^c\, t_k^c\, d_l^c) \tag{26}$$

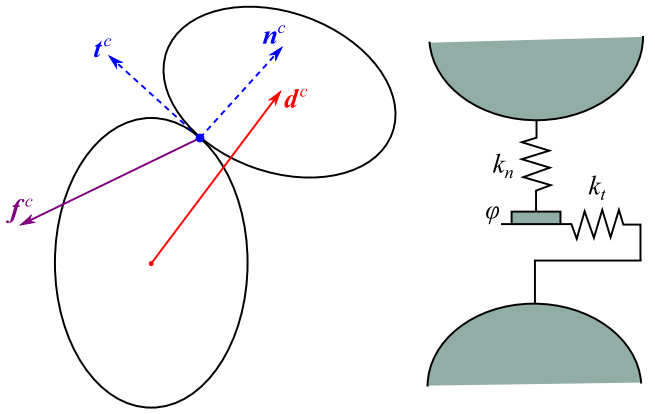

Fig. 1. Contact geometry and contact law for DEM model.

where n_i^c and t_i^c are the unit normal and the tangential vectors at a contact, respectively (see Fig. 1); k_n and k_t are the normal and the tangential stiffnesses which describe the interparticle contact law in the DEM solver. In the current study, a linear force–displacement contact law is adopted in conjunction with the Coulomb's friction criterion defined by the interparticle contact friction angle φ. k_n and k_t are determined from another two input parameters E_c and ν_c

$$k_n = E_c\, r^* \tag{27}$$

$$k_t = \nu_c\, k_n \tag{28}$$

where r^* $(=2\, r_1 r_2/(r_1 + r_2))$ is the common radius of the two contacting particles with radii r_1 and r_2, respectively. In addition, a damping force is added to each particle to ensure the quasi-static condition. Its direction is opposite to the particle velocity and its magnitude proportional to the unbalanced force of the particle with a constant damping ratio β. E_c, ν_c, φ, β, along with the particle size distribution, and the particle density ρ_p are typical user defined input parameters in the DEM solver. For more details about the DEM model, interested readers are referred to the `YADE` documentation [40].

2.4. Iterative coupling, solution procedure and parallelisation

2.4.1. Fixed-stress split method

To solve Eqs. (1) and (3), we employ the sequential iterative scheme, a variation of the Gauss–Seidel method, to tackle the coupling. Specifically, a so-called "fixed-stress split" method is adopted following Refs. [31–33] which is proved to be unconditionally stable when $0.5 \leq \theta \leq 1$ and offers better performance in terms of convergence rate, stability and accuracy compared with other split methods [31,33,41]. Particularly in the fixed-stress split method, while assumptions are made in the fluid solver (constant total stress rate), the mechanical solver retains its original form. It means we are able to directly apply our earlier hierarchical multiscale approach for dry granular media [13–17] as the mechanical solver here. Notably, however, in some other split methods, such as the undrained split method [32], though being unconditionally stable when $0.5 \leq \theta \leq 1$, the drained tangent modulus C_{ijkl} expressed in Eq. (26) needs to be replaced by the undrained one $(C_{ijkl} + K_f/n\, \delta_{ij}\delta_{kl})$ when it is used in Eq. (17) to assemble the stiffness matrix.

The fixed-stress split method can be expressed as

$$\begin{bmatrix} \mathbf{u}^{(n)} \\ p^{(n)} \end{bmatrix} \xrightarrow{\mathcal{A}^p} \begin{bmatrix} \mathbf{u}^{(*)} \\ p^{(n+1)} \end{bmatrix} \xrightarrow{\mathcal{A}^u} \begin{bmatrix} \mathbf{u}^{(n+1)} \\ p^{(n+1)} \end{bmatrix} \tag{29}$$

where $\mathcal{A}^p$ and $\mathcal{A}^u$ are two split operators. In $\mathcal{A}^p$, the pore fluid pressure is solved by assuming the total stress rate is constant, i.e. $\delta\dot{\sigma}_{ij} = 0$. The volumetric strain rate in Eq. (3) is calculated

$$\dot{\varepsilon}_v = \frac{\dot{\sigma}'_v}{K_{dr}} = \frac{\dot{\sigma}_v + \alpha\, \dot{p}}{K_{dr}} \tag{30}$$

where σ_v (σ_v') is the mean total (effective) stress, K_{dr} is the drained bulk modulus, which can be estimated from the tangent modulus of the solid matrix

$$K_{dr} = \frac{1}{\delta_{mm}^2}\,\delta_{ij}\,C_{ijkl}\,\delta_{kl} \tag{31}$$

where in the coefficient, $\delta_{mm} = 2$ for 2D problems and $\delta_{mm} = 3$ in 3D cases.

From Eq. (30), the assumption of constant total stress rate suggests that during each iteration

$$\varepsilon_v^{(n+1,k+1)} - \varepsilon_v^{(n+1,k)} = \frac{\alpha}{K_{dr}}(p^{(n+1,k+1)} - p^{(n+1,k)}) \tag{32}$$

where the superscripts (k) and $(k+1)$ denote two consecutive iterations. The iteration of Eq. (3) can then be written as

$$[k_{ij}(-p_{,j}^{(n+1,k+1)} + \rho_f\, b_j)]_{,i} + \left(\frac{n}{K_f} + \frac{\alpha^2}{K_{dr}}\right)\frac{p^{(n+1,k+1)}}{\Delta t} = \frac{n}{K_f}\frac{p^{(n)}}{\Delta t} + \frac{\alpha^2}{K_{dr}}\frac{p^{(n+1,k)}}{\Delta t} - \frac{\alpha\,\varepsilon_v^{(n+1,k)}}{\Delta t}. \tag{33}$$

With updated $p^{(n+1,k+1)}$, $\mathbf{u}^{(n+1,k+1)}$ can be easily obtained in $\mathcal{A}^u$ from the mechanical solver

$$(C_{ijkl}\varepsilon_{kl}^{(n+1,k+1)} + \sigma'^{(n)}_{ij} - \alpha\, p^{(n+1,k+1)}\delta_{ij})_{,j} + \rho\, b_i = 0. \tag{34}$$

Note that there is no need to explicitly solve the intermediate displacement $\mathbf{u}^{(*)}$ in Eq. (29) during the iteration.

2.4.2. *Flowchart of the coupled hierarchical multiscale approach*

The solution procedure for the coupled hydro-mechanical problem is summarised by the flowchart in Fig. 2. At the global level, the Gauss–Seidel-like iteration is used in conjunction with the fixed-stress split method to find the converged solution of the solid displacement and the pore fluid pressure. The convergence criterion is given as:

$$\frac{\|\mathbf{u}^{(n+1,k+1)} - \mathbf{u}^{(n+1,k)}\|_2}{\|\mathbf{u}^{(n+1,k+1)}\|_2} \le \mathrm{TOL}_u \tag{35}$$

$$\frac{\|p^{(n+1,k+1)} - p^{(n+1,k)}\|_2}{\|p^{(n+1,k+1)}\|_2} \le \mathrm{TOL}_p. \tag{36}$$

The values of TOL_u and TOL_p are both set to be 10^{-3} in the study. Note that Newton–Raphson iteration is adopted in the mechanical solver in Fig. 2 to tackle the material nonlinearity in the hierarchical multiscale approach. The convergence criterion for the mechanical solver has been previously given in Eq. (20). Compared with the linear convergence performance observed for the local Newton–Raphson scheme [14], the global Gauss–Seidel iterative scheme is much more efficient [31,33], usually reaching a converged solution within 5 iterations.

2.4.3. *Parallelisation*

It is quickly realised that the local DEM computations are so time-consuming that it may potentially impede any practical application of the proposed multiscale approach. For a medium-sized coupled hydro-mechanical problem, hundreds to thousands (equal to the number of Gauss points) of independent DEM solvers need to be invoked within two nested iterative schemes (global Gauss–Seidel and local Newton–Raphson). The heavy computational cost can indeed be effectively relieved by parallel DEM solvers by virtue of the hierarchical structure of the approach. In our previous work [13–17], the code has been parallelised to run on a multi-core processor. However, there was an obvious bottleneck that constrains the scalability of the parallelisation due to limited number of cores in the single computing node. To overcome this limit, the message passing interface (MPI) [42] has been implemented in the current code to run the separate DEM computations in parallel on a high-performance computing (HPC) cluster. Fig. 3(a) shows the identical axial stress–strain responses of a drained biaxial compression test (without considering water, same as that presented in Ref. [14]) by using different numbers of computing nodes. Fig. 3(b) demonstrates a nearly linear scalability of the parallelisation, i.e. the spent user time (total time includes both computational costs for DEM and FEM) halves when the number of node doubles. It is also seen from Fig. 3(b) that the drained test without considering water can generally finish within a few hours. For the undrained test considering hydro-mechanical coupling in the

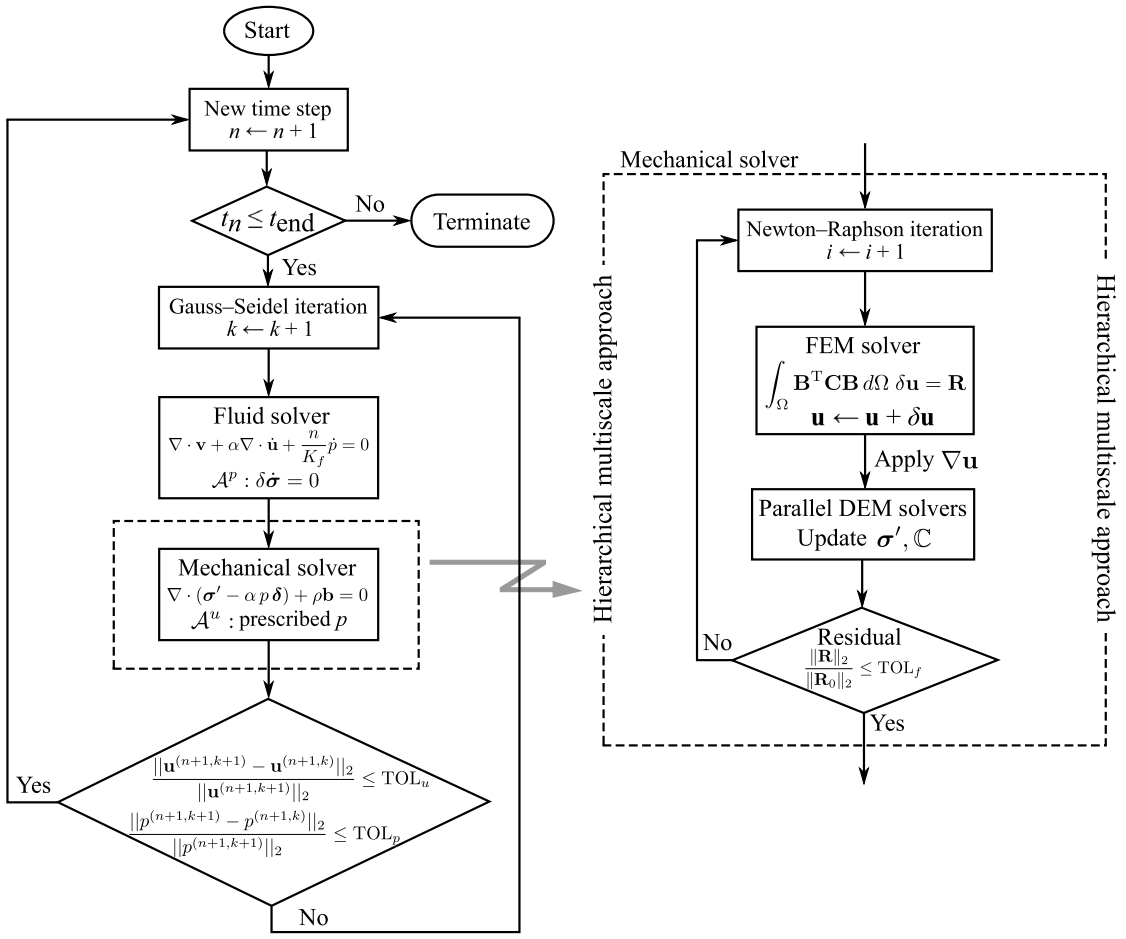

Fig. 2. Flowchart for the global solution procedure and the mechanical solver (in dashed box).

present study, the computation takes much longer time. Using available 4 HP ProLiant SL250 Gen8 nodes and a total of 80 cores (each node has 2 × 10-core 2.2 GHz CPU and 64 G RAM), a globally undrained biaxial compression test containing 512 embedded RVE packings (a total of 204,800 particles for the whole problem domain), as to be presented in Section 4, costs around 80 h.

3. Benchmark

In this section, we employ the following two classical geomechanics problems for which closed-form solutions are available to benchmark our implementation of the coupled hierarchical multiscale approach—the Terzaghi's 1D consolidation problem and the 2D consolidation under a strip footing.

3.1. RVE and material parameters

Following the procedure outlined in Ref. [14], we adopt a typical RVE packing containing 400 circular particles, as shown in Fig. 4(a). For the sake of simplicity, complex particle shape or contact rolling resistance is not considered here. The parameters used for the subsequent simulations are summarised in Table 1. Periodic boundary is applied on both directions of the RVE. The RVE packing possesses an initial mean effective stress $\sigma'_{v0} = -100$ kPa and a porosity about $n_0 \approx 0.15$. The range of porosity of the RVE packing is found being able to vary between 0.147 and 0.2. Hence, the adopted RVE can be treated as initially dense. We further assume the pore-filled fluid is water with $K_f = 2.2$ GPa and $\mu_f = 8.9 \times 10^{-4}$ Pa s at room temperature, and the average diameter of the modelled sand grain is $\bar{d} = 0.001$ m. The permeability of the sand is then estimated as $k \approx 2.9 \times 10^{-8}$ m^2/(Pa s) from Eq. (4).

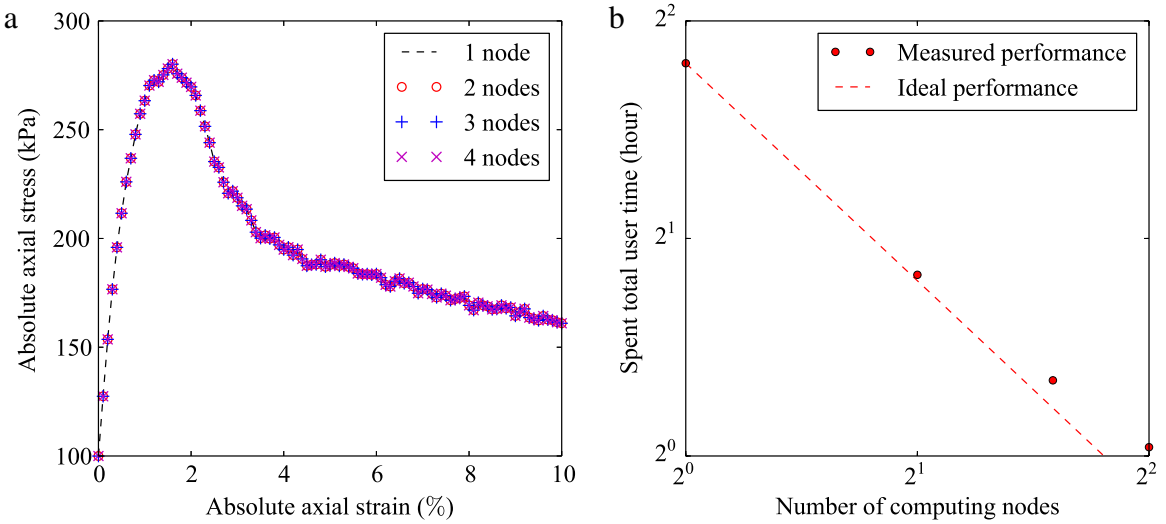

Fig. 3. (a) Comparison of simulation results from a drained biaxial compression test using different number of computing nodes; (b) spent total user time against number of computing nodes.

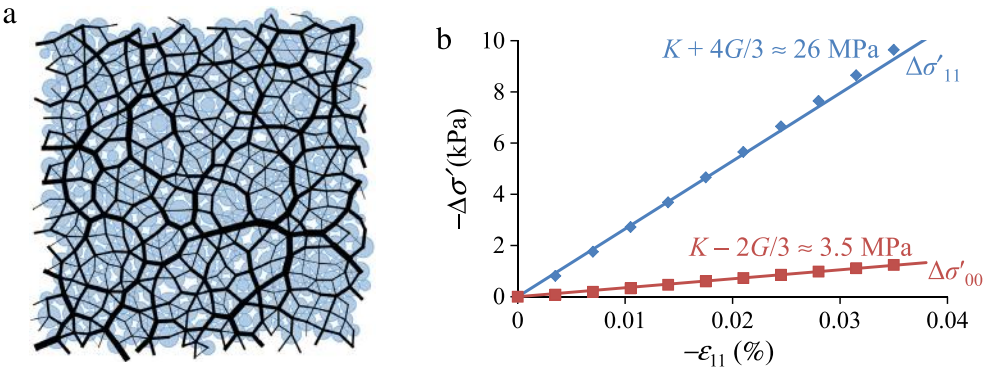

Fig. 4. (a) Prepared RVE packing with an isotropic mean effective stress of −100 kPa; (b) Elasticity parameters of the soil matrix determined from the unit-cell dry œdometer test at small strains.

Table 1
Parameters for the DEM RVE.

Particle radii (mm)[a]	ρ_p (kg/m^3)	E_c (MPa)	ν_c	φ (rad)	β
3 ∼ 7	2650	600	0.8	0.5	0.1

[a] The particle size in the DEM model is scaled-up to achieve computational efficiency.

To obtain the analytical solutions for benchmarking, the elasticity parameters are also required. 1D compression (œdometer) test is hence performed on a single element at small strains (absolute axial strain less than 0.04%, dry unit-cell test). The slopes of the two stress–strain lines in Fig. 4(b) offer the following relations $\Delta\sigma'_{11}/\Delta\varepsilon_{11} = K + 4G/3$ and $\Delta\sigma'_{00}/\Delta\varepsilon_{11} = K - 2G/3$, where K and G are the bulk and the shear moduli of the soil matrix, respectively. They are estimated from Fig. 4(b) as $K \approx 11$ MPa and $G \approx 11.3$ MPa, which will be used to determine the coefficient of consolidation in the analytical solutions.

3.2. 1D consolidation of an elastic soil

A soil column with an initial height of $H = 10$ m is discretised with a coarse mesh using 1×10 quadrilateral elements as shown in Fig. 5. Each element contains 8 displacement nodes and 4 pressure nodes (Q8P4 element). We

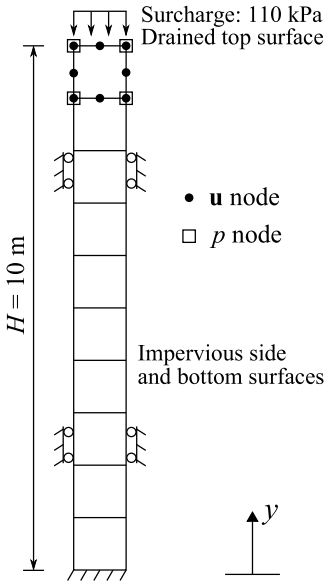

Fig. 5. Mesh and boundary conditions for the 1D consolidation problem.

employ a reduced integration scheme which requires 4 RVE packings for each element. The same element type and integration technique was adopted by other researchers studying water-saturated elasto-viscoplastic soils [43,44], and will be used in all the tests throughout the paper. Regarding the boundary conditions, the bottom of the column is fixed in space; while the side boundaries are fixed in the horizontal direction and are free to move vertically. Body force is neglected. To ensure the soil only undergoes elastic deformation, a constant surcharge of 110 kPa which is slightly larger than the initial mean effective stress of the soil matrix ($\sigma'_{v0} = -100$ kPa) is applied on the top end of the column. The initial pore water pressure throughout the domain is assumed uniform with a magnitude of $p_0 = 10$ kPa to ensure the soil column is initially in equilibrium. At time $t = 0$, the top surface is allowed to drain ($p = 0$) while the two side walls and the bottom end are kept impervious. It is expected when the pore water pressure is totally dissipated and a new equilibrium is reached, the vertical effective stress increment of the soil matrix is $\Delta\sigma'_{11} = -p_0 = -10$ kPa. According to Fig. 4(b), the soil remains in its elastic regime at this small stress increment.

We use a non-dimensional time measure T defined as $T = ct/H^2$ for the following discussion, where the coefficient of consolidation c can be estimated from the fitted elastic moduli as $c = k/(n/K_f + 1/(K + 4G/3)) \approx 0.75$. The time step ΔT in the computation varies from 0.02 to 0.5. Fig. 6 presents the temporal evolution of the pore water pressure distribution along the column and the degree of consolidation U defined as $U = (u_t - u_0)/(u_\infty - u_0)$, where u_0, u_t and u_∞ are the immediate surface settlement, and the settlements at time t and infinite time, respectively. The analytical solutions [2,45] are shown in solid lines for comparisons. It is found the numerical predictions generally agree with the analytical solutions.

3.3. 2D consolidation of an elastic soil

The model is further validated with the 2D consolidation problem under a strip footing. Due to the symmetry of the problem, only half of the domain is modelled as shown in Fig. 7. A coarse mesh with 14×5 unevenly distributed Q8P4 elements is generated using the open-source mesh generator `Gmsh` [46]. The height and the half length of the domain are 1 m and 15 m, respectively. The (flexible) footing is modelled as a surcharge $f = 110$ kPa with a half width $b = 1$ m. The solid matrix is assumed to have an initial mean effective stress $\sigma'_{v0} = -100$ kPa. A confining pressure of the same magnitude is applied to the top surface except the footing area. The left and the right boundaries are fixed in the horizontal direction, and the bottom is fixed in vertical. Only the top surface is assumed to be drained, while all the other boundaries are assumed impervious. The gravity is neglected. We use a similar non-dimensional time measure $T = ct/b^2$ defined in the 1D case for the following discussion. The time step ΔT also varies from 0.02 to 0.5 in the test. The time histories of the normalised settlement right below the centre of the footing defined

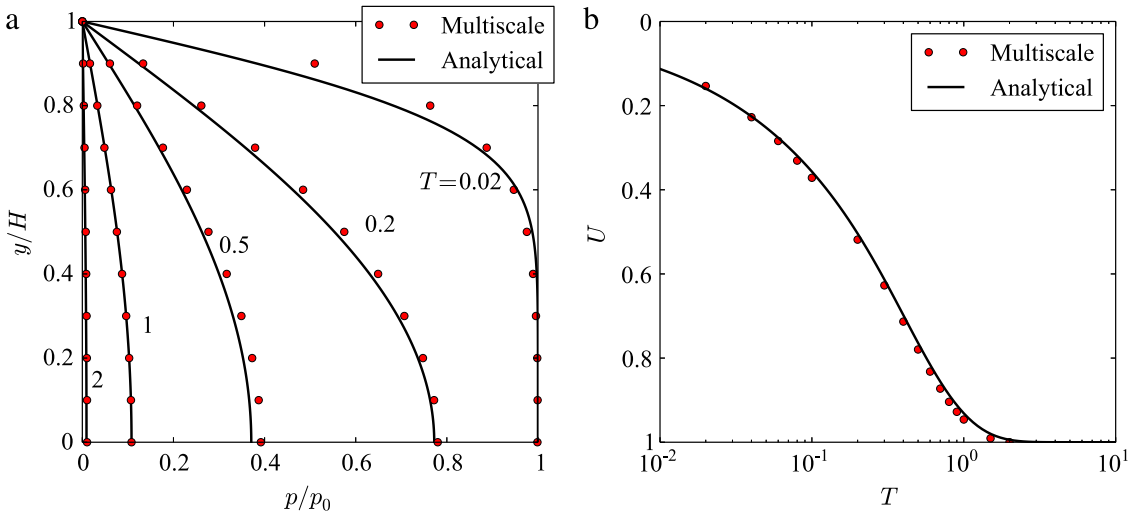

Fig. 6. Temporal evolutions of (a) the pore water pressure distribution and (b) the degree of consolidation for the 1D consolidation problem.

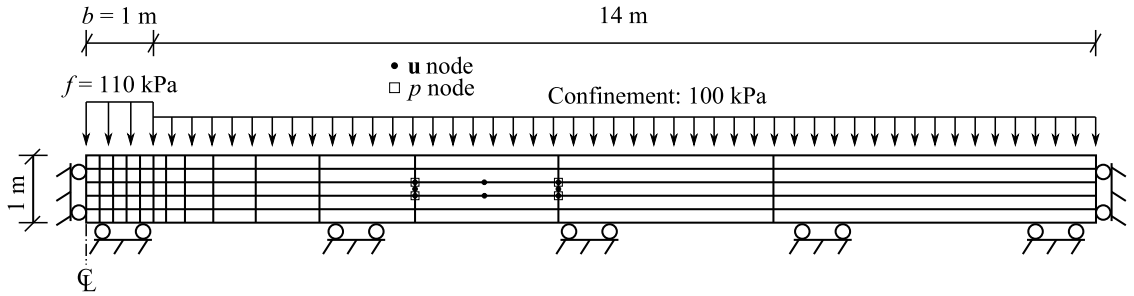

Fig. 7. Mesh and boundary conditions for the 2D consolidation problem.

by $\bar{u} = Gu/[(f + \sigma'_{v0})b]$ and the pore water pressure at the node 0.6 m beneath the centre of the footing are plotted in Fig. 8. Compared in the figure is the analytical solution of the settlement from Ref. [47] using a Poisson's ratio $\nu = 0.12$ ($\nu = (3K - 2G)/(6K + 2G)$). While no analytical solution for the pore water pressure is available in the literature, our multiscale simulation captures a slight increase of p during the early stage of consolidation (the trend is marked by a small arrow in Fig. 8(b)) then followed by a steady drop at the monitored node, which is known as the Mandel–Cryer effect [48,49]. It is noted that the numerical results for the settlement and the pore water pressure at small T can be further improved, e.g., by refining the mesh and increasing the length of the domain.

4. Globally undrained biaxial compression tests

In this section, the coupled hierarchical multiscale approach is further employed to simulate globally undrained biaxial compression tests on two specimens of the same dimension of 50 mm × 100 mm but with different initial densities. The domain is discretised into 8 × 16 Q8P4 elements as shown in Fig. 9. The top and the bottom surfaces are assumed smooth. A uniform vertical displacement is applied to the top surface to load the specimens axially. To approximate the quasi-static loading, the axial strain rate is controlled at $\dot{\varepsilon}_{11} = -5 \times 10^{-7}\ \mathrm{s}^{-1}$ (-0.18%/hour, see also Refs. [50,51]). The time step is set to $\Delta t = 100$ s. The specimens have an identical initial isotropic effective stress of -100 kPa and the initial pore water pressure is uniformly set to 0 kPa. No cavitation [51,52] has been spotted during the loading process (p stays above -100 kPa, see Fig. 12). A constant confining pressure of $\sigma_{00} = -100$ kPa is exerted on the left and the right surfaces of the specimen. All the boundaries are impervious to achieve the globally undrained condition for the compression tests, while local drainage is allowed. We examine the influence of the initial density by considering a dense case and a loose case. For the dense specimen, we use the same RVE as that in Section 3, which has an initial porosity of $n_0 = 0.15$ and an initial permeability of $k_0 = 2.9 \times 10^{-8}\ \mathrm{m}^2/(\mathrm{Pa\,s})$; while for the loose

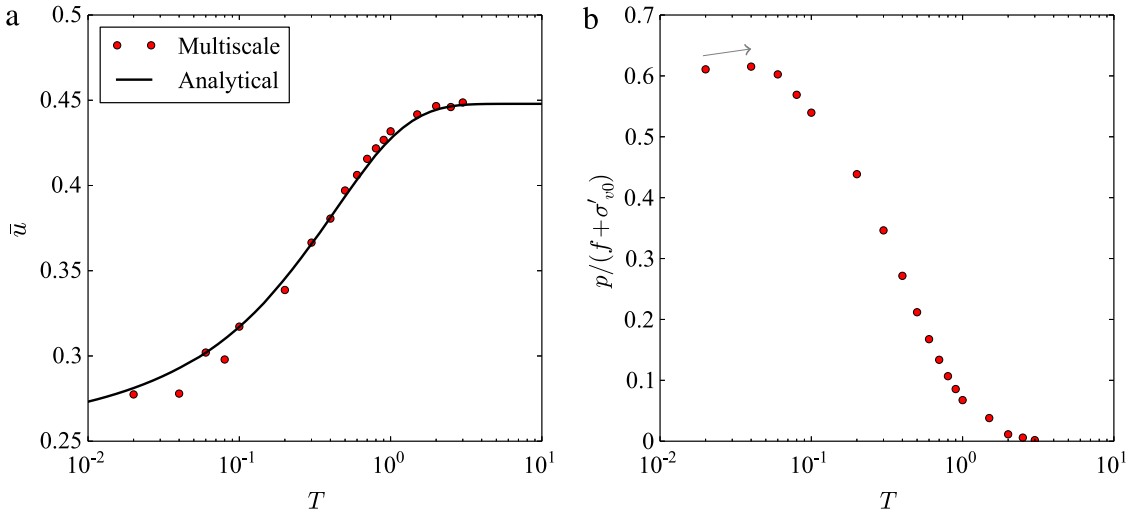

Fig. 8. Temporal evolutions of (a) the normalised soil settlement at the centre of the footing and (b) the pore water pressure at the node 0.6 m beneath the centre of the footing.

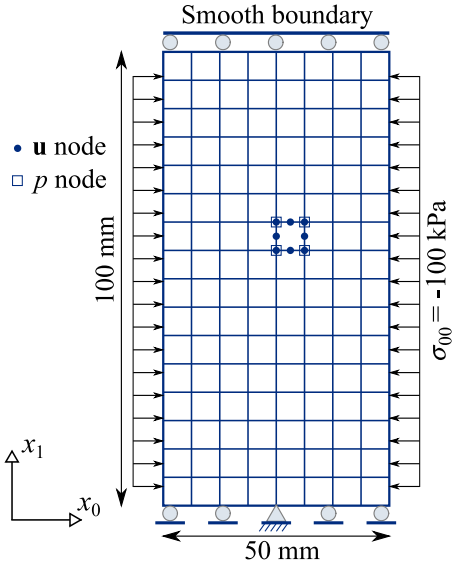

Fig. 9. Mesh and boundary conditions for the globally undrained biaxial compression tests.

specimen, considering its coordination number (contact number per particle) is low, we use 800 particles in the RVE and prepare the RVE with an initial porosity of $n_0 = 0.189$. The material parameters for both RVEs still follow those listed in Table 1. With $\bar{d} = 0.001$ m, the loose specimen has an initial permeability of $k_0 = 6.4 \times 10^{-8}$ m^2/(Pa s) according to Eq. (4).

4.1. Responses of effective stress–strain and pore water pressure

Fig. 10 presents the evolution of the effective axial stress exerted on the loading platen against the nominal axial strain for the dense specimen. The result from a separate dry DEM test on the RVE packing sheared under the constant volume condition is also presented for comparison. It is seen the two results are very close when the axial strain is small ($|\varepsilon_{11}| < 1\%$). When $1\% < |\varepsilon_{11}| < 2\%$, the effective axial stress from the coupled hydro-mechanical multiscale simulation is slightly smaller than that from the dry DEM test. Indeed from the later local analyses (see Section 4.3), $\varepsilon_{11} = -1\%$ can be regarded as the onset of strain localisation. A marked difference between the two is observed

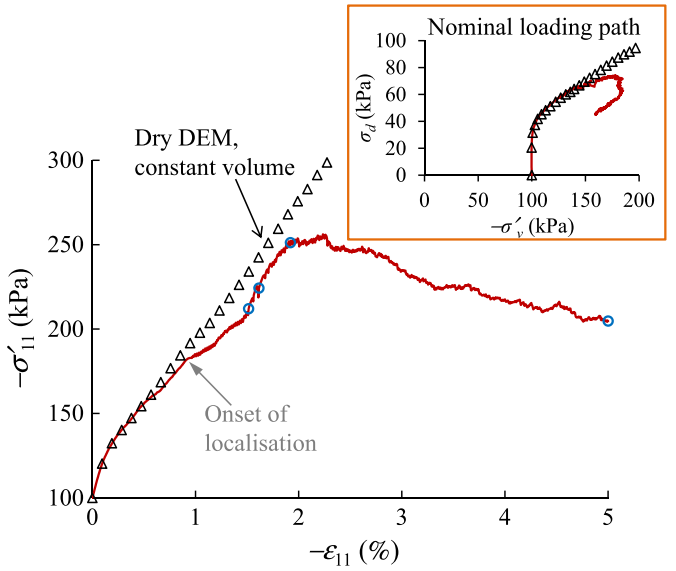

Fig. 10. Effective axial stress versus nominal axial strain for the dense specimen (solid line) compared with the dry DEM test on its RVE under the constant volume condition (open triangle). The inset shows the nominal loading path of the whole specimen.

when $|\varepsilon_{11}| > 2\%$. While the DEM result shows a continuous hardening process, the multiscale test shows a softening response. The hardening followed by softening response of the multiscale test can also be seen from the nominal loading path of the whole specimen shown in the inset of Fig. 10, where unlike the continuous hardening DEM loading path, apparent decreases of magnitudes in both mean effective stress σ'_v and deviatoric stress σ_d are found after the peak stress state. This softening observed at large strain levels is attributable to the formation of well-developed shear band in the dense specimen which will be discussed in Section 4.2. Notably, a similar pull back of effective stress path towards the final loading stage due to localisation has also been observed in laboratory tests [53] and other numerical simulations [54].

The responses of the loose specimen are presented in Fig. 11. The multiscale simulation shows a very similar result as compared to the constant-volume, dry DEM test case, i.e., a small increase of effective axial stress at the beginning of loading, followed by a severe stress reduction towards the final state. At about $\varepsilon_{11} = -4\%$, the decrease of $|\sigma'_{11}|$ is so dramatic that no converged solution can be reached, which forces termination of the computation. A typical flow failure has been observed and the specimen becomes severely deflected due to its loss of strength (see Section 4.2). The final state can hence be treated as the liquefaction state for the loose specimen. The trend towards liquefaction can also be observed from the softening loading path of the specimen from the inset of Fig. 11.

The pore water pressure fields for both specimens are found rather uniform over the entire domain during the loading process even when shear localisation occurs. The measured coefficient of variation (the ratio of the standard deviation and the mean) of p over the domain stays below 10^{-5}. Thus, we are able to use the domain-averaged p for the whole specimen and plot the evolutions of p for both specimens in Fig. 12. For the dense specimen, the pore water pressure has a fast initial increase, up to a peak value of 37 kPa at $\varepsilon_{11} = -0.4\%$. After the peak, it gradually decreases due to the dilation of the dense packing. Since the onset of localisation ($\varepsilon_{11} = -1\%$), the response of the pore water pressure becomes slightly fluctuated. At around $\varepsilon_{11} = -1.5\%$, a deflection point (a significant changing of the slope of the curve, shown as the leftmost circle marker on Figs. 10 and 12 for σ'_{11} and p, respectively) is observed. A clear flow pattern is actually observed at this stage (see Fig. 13(a)). After about $\varepsilon_{11} = -3\%$, p increases mildly again due to the localisation-induced softening. However, the shear strain level for p to increase is higher than that for $|\sigma'_{11}|$ to decrease by comparing Figs. 10 and 12. For the loose specimen, p increases steadily up to 67.5 kPa at about $\varepsilon_{11} = -4\%$ followed by an abrupt build up of p, which leads to the final liquefaction of the loose packing.

4.2. *Deformation and flow patterns*

Four characteristic stages during the loading course (sequentially marked by empty circles in Figs. 10 and 12) are selected to examine the deformation and flow patterns of the dense specimen. Shown in Fig. 13 are the porosity

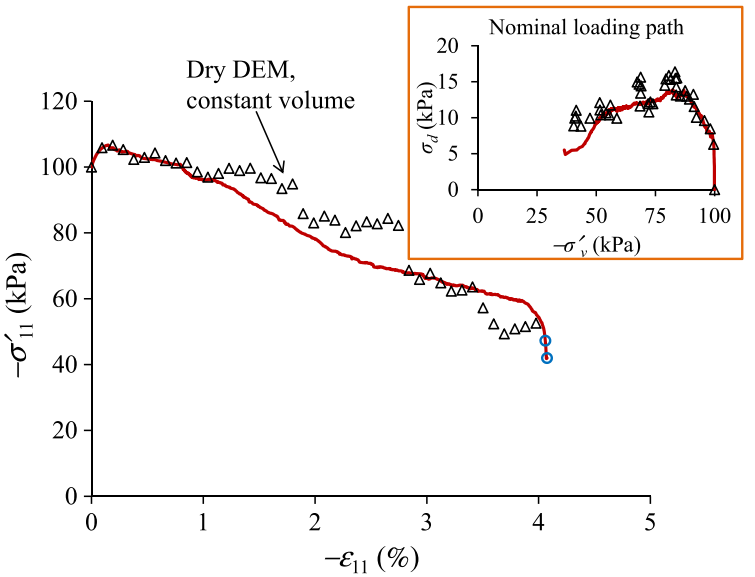

Fig. 11. Effective axial stress versus nominal axial strain for the loose specimen (solid line) as compared with the dry DEM test on its RVE under the constant volume condition (open triangle). The inset shows the nominal loading path of the whole specimen.

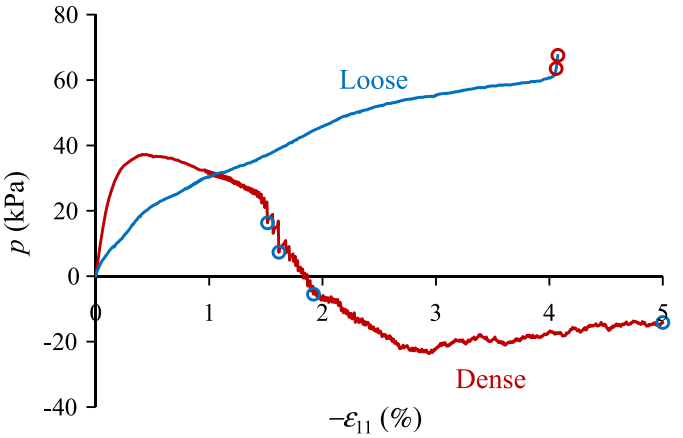

Fig. 12. Evolutions of pore water pressure of the dense and the loose specimens.

contour and the Darcy flux ($v_i = k_{ij}(-p_{,j} + \rho_f b_j)$) field at the selected four strain levels. During the initiation stage of strain localisation ($1\% < |\varepsilon_{11}| < 1.5\%$), the variation of the porosity field is vanishingly small, and the Darcy flux is rather weak too and nearly negligible. At the deflection point ($\varepsilon_{11} = -1.515\%$), there appears a clear flow pattern showing that the water flows into a banding area. The analysis of our data indicates this is the first time that a clear flow pattern can be identifiable. However, at this stage, strain localisation remains not obvious as the porosity contour stays relatively uniform. The state with the most significant Darcy flux occurs at $\varepsilon_{11} = -1.615\%$, where mild drops of $|\sigma'_{11}|$ and p are observed from Figs. 10 and 12, respectively. The flow pattern is similar to that shown at the deflection point but with much larger magnitudes. The localisation pattern remains weak though at this state. Interestingly, after this stage, the flow pattern nearly disappears as seen from Fig. 13(c) ($\varepsilon_{11} = -1.92\%$, a state close to the peak effective stress state). Nevertheless, the localisation pattern at this stage is more intense than before, with a well-developed persistent shear band becoming apparent. At the final loading stage ($\varepsilon_{11} = -5\%$), the full-fledged shear band is clearly observed with near-zero Darcy flux over the entire domain. For the dense specimen case, the shear band is notably dilative in nature. The expansion of pores inside the shear band also causes a great increase in the permeability therein according to the Kozeny–Carman equation (Eq. (4)), which constitutes the major driving

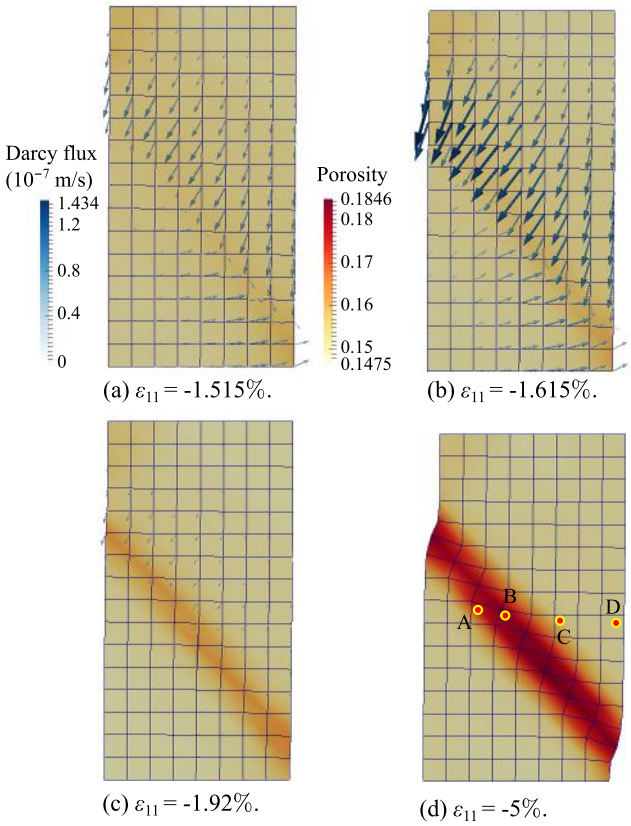

Fig. 13. Superimposed strain localisation and flow patterns of the dense specimen at different shearing levels. Stronger flux corresponds to thicker and longer arrows in the figure. The four Gauss points marked in (d) will be used for local analyses in Section 4.3.

mechanism for the occurrence of in-band flow pattern during the loading. Indeed, spatial variation of porosity induced by the external load is key for the interesting flow patterns to be captured. The delayed occurrence of the first apparent flow (at $\varepsilon_{11} = -1.515\%$) as compared to the onset of localisation (at $\varepsilon_{11} = -1\%$) indeed is due to the requirement of certain degree of dilation inside the localised zone to trigger the porosity difference and hence induce a high enough pressure gradient over the domain. Due to the quasi-static loading condition, the Darcy flux magnitude is generally small, in the order of 10^{-7} m/s according to our simulations.

Fig. 14 shows the contours of pore water pressure at the selected four stages. The first three stages correspond to relatively inhomogeneous distribution of pore water pressure in the specimen, albeit with rather small pressure gradient (noting the value range of the colour-map is narrow). No pressure gradient is found at $\varepsilon_{11} = -5\%$ when the Darcy flux totally disappears. Notably, at $\varepsilon_{11} = -1.615\%$ when the Darcy flux is most distinct, a relatively larger pressure gradient than the other cases is appreciable across the shear band region.

For the loose specimen, since the deformation in all preceding stages are relatively homogeneous, we select two stages close to the end of loading as marked in Fig. 11. It is evident from Fig. 15 that severe deflection occurs to the specimen at the two stages. From the final drastic decrease of axial stress shown in Fig. 11 and the severe deflection of sample shown in Fig. 15, the loose specimen is expected to collapse due to the liquefaction-induced loss of strength. Similar observations of the diffuse failure modes of loose sands were found in experiments [55,56]. The porosity field in the specimen is relatively uniform except some mild strain concentration at the lower-left and the upper-right corners due primarily to the boundary constraints when the sample undergoes lateral distortion. In contrast to the localised failure in the dense specimen, the loose specimen fails rather diffusely with no obvious shear localisation. No identifiable flow pattern is observed throughout the loading process until the final failure stage ($\varepsilon_{11} = -4.075\%$) when mild flows point to the strain-concentrated corner areas. Meanwhile, the loose specimen experiences largely steady contraction across the specimen except at the two corners. Both the porosity and the permeability are hence

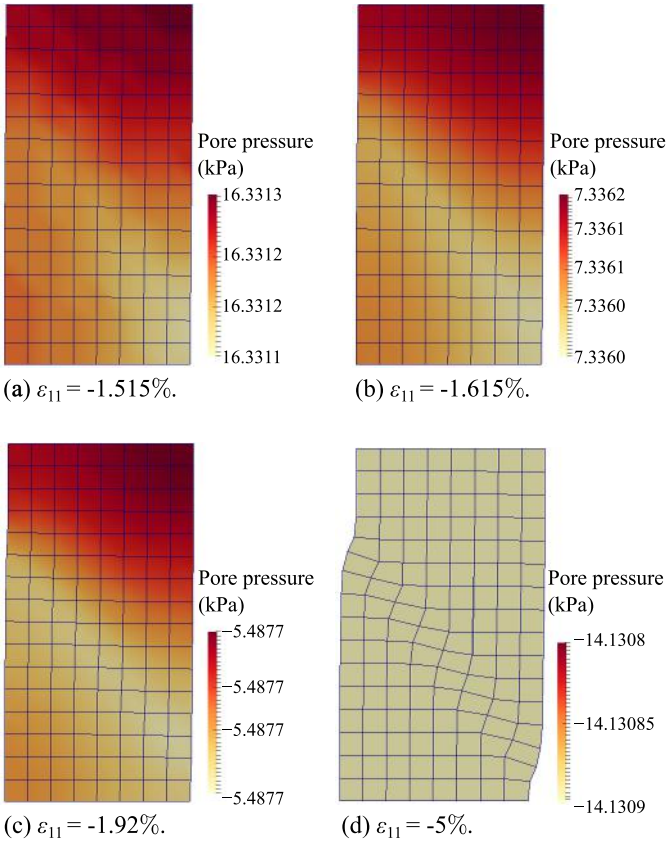

Fig. 14. Contours of pore water pressure of the dense specimen at different shearing levels.

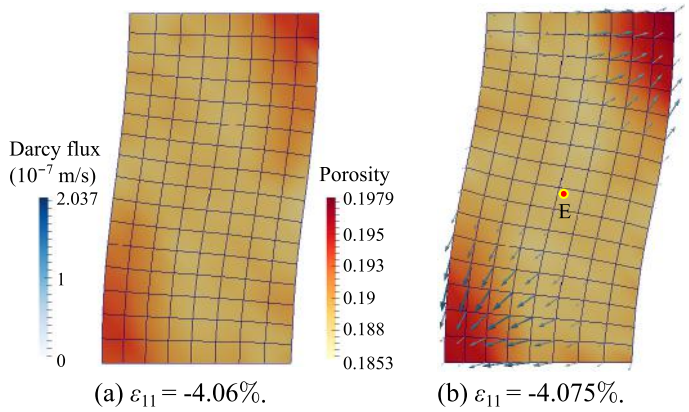

Fig. 15. The deformation and flow patterns of the loose specimen at final loading stages showing deflection and diffuse liquefaction. The marked Gauss point in (b) will be used for local analyses in Section 4.3.

smaller than in the corner areas, which causes the water flowing from the central region into the two corners at $\varepsilon_{11} = -4.075\%$. Similar to the dense case, the magnitude of Darcy flux is in the order of 10^{-7} m/s. The contours of pore water pressure at these two stages, shown in Fig. 16, indicate a rather uniform pressure field without apparent pressure gradient at both strain levels.

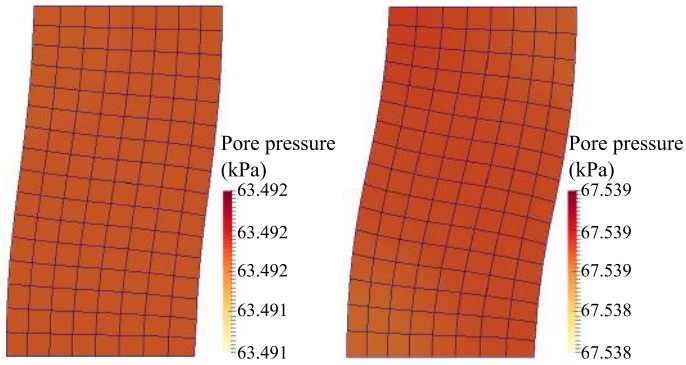

Fig. 16. Contours of pore water pressure of the loose specimen at final loading stages.

4.3. Cross-scale analyses

To gain deeper understanding of the macroscopic observations, we may directly examine their underlying microscopic mechanisms by virtue of the hierarchical structure of the multiscale modelling framework. A number of typical Gauss points from the problem domain are selected for the cross-scale analyses. In the case of the dense specimen, four material points initially located at the same height of the specimen are chosen, labelled in Fig. 13(d) as A, B, C and D, respectively. Points A and B are located inside the final shear band (A is right inside the boundary and B is close to the centre); Point C is located close to the outside edge of the shear band; and point D is totally outside the shear band.

We first investigate the local material responses of the four chosen points, as presented in Fig. 17. Prior to $\varepsilon_{11} = -1.5\%$, all four material points show an identical hardening behaviour as seen from their evolution curves of σ_d (Fig. 17(a)) and loading paths (Fig. 17(b)). However their responses start to bifurcate after $\varepsilon_{11} = -1.5\%$. Points A and B both undergo shear softening responses due to significant volume dilation caused by strain localisation (see Fig. 17(d)). Point D also shows a similar decrease in both deviatoric stress and mean effective stress, due not to softening as for the cases of A and B, but primarily caused by an unloading process indicated by the inset of Fig. 17(c) showing its shear strain drops from a peak value of 3.2% to about 2.3%. While the softening responses of A and B appear to be rather fluctuated, the unloading response at point D is relatively smooth (Fig. 17(a)). Fig. 17(c) also indicates that the shear strain levels at A and B continue to increase substantially. As point B is located in the centre of the shear band, it undergoes the most intensive shearing, reaching $\varepsilon_d = 83\%$ at the final stage. The final shear strain at point A is about 24.7%. Comparatively, the shearing levels of the two points outside the shear band are rather small, both below 3.5%. Although the specimen is sheared under a globally undrained condition, Fig. 17(d) indicates rather significant local volume changes occurring in the specimen. Before the onset of localisation ($\varepsilon_{11} = -1\%$), no apparent volumetric deformation is observed for all four Gauss points. Once strain localisation is initiated, all four material points first show a volume dilation during the initiation stage of the shear band. The two points inside the shear band indeed undergo a large volume dilation, reaching $\varepsilon_v = 3.7\%$ and 4.5% at the final state, respectively. The two points outside the shear band begin to contract after $\varepsilon_{11} = -1.5\%$ (the first stage to observe the flow pattern). Point C shows an overall contractive response with a final $\varepsilon_v = -0.3\%$. Due to the unloading process, ε_v at point D totally vanishes towards the end. A further scrutiny of the responses of point C shows that it undergoes pure contraction after $\varepsilon_{11} = -1.5\%$, as its shear strain level is maintained constant at about $\varepsilon_d = 3.5\%$ according to the inset of Fig. 17(c). Since point C is close to the edge of the shear band, the volume contraction is attributable to the water flow out of this point into the shear band after $\varepsilon_{11} = -1.5\%$ (see Fig. 13). The volume contraction also contributes to the hardening response at point C without apparent stress drop as shown in Fig. 17(a) and (b), which is rather different from the other three points.

The interesting responses of point C inspire us to examine other material points located close to the edge of the shear band. Their responses are collectively plotted in Fig. 18(a) and their locations are marked in the deformed mesh shown in Fig. 18(b). These points indeed show similar and consistent responses. At the onset of localisation, the points at the upper edge of the shear band first depict an acute increase in deviatoric strain. The jumps of ε_d for the points

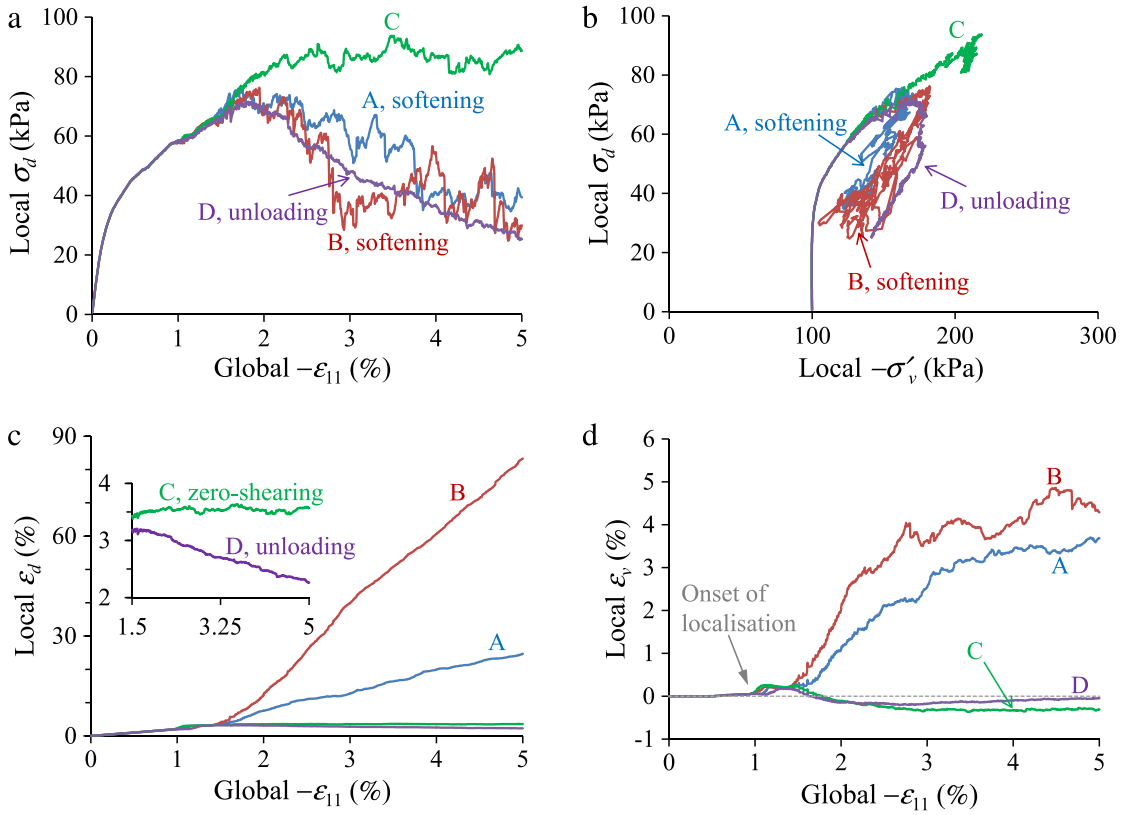

Fig. 17. Selected local material responses of the dense specimen: (a) evolutions of deviatoric stress; (b) loading paths; (c) and (d) evolutions of deviatoric strain and volumetric strain.

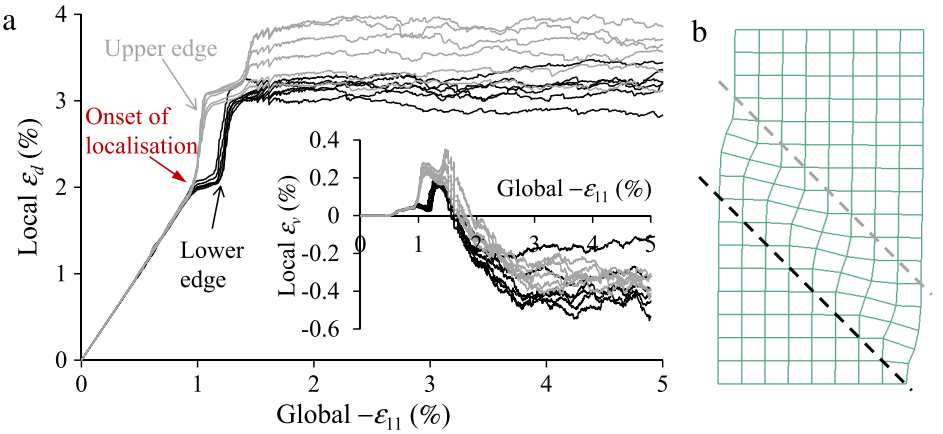

Fig. 18. Responses of material points close to the upper and the lower edges (positions shown in (b)) of the shear band.

at the lower edge are slightly lagging behind. After $\varepsilon_{11} = -1.5\%$, the deviatoric strain levels of all these points stay roughly unchanged, indicating no further shearing occurring to these points. From the inset of Fig. 18(a), it is found that their volumes dilate abruptly at around $\varepsilon_{11} = -1\%$ (the points at the upper edge dilate earlier than those at the lower edge). After $\varepsilon_{11} = -1.5\%$, due to the water flow out of these points, their volumes begin to contract as ε_v changes from positive to negative. Their volumetric strains stay roughly constant after $\varepsilon_{11} = -3\%$ as the deformation is mainly concentrated within the shear band, and no water flow takes place at large shearing strains.

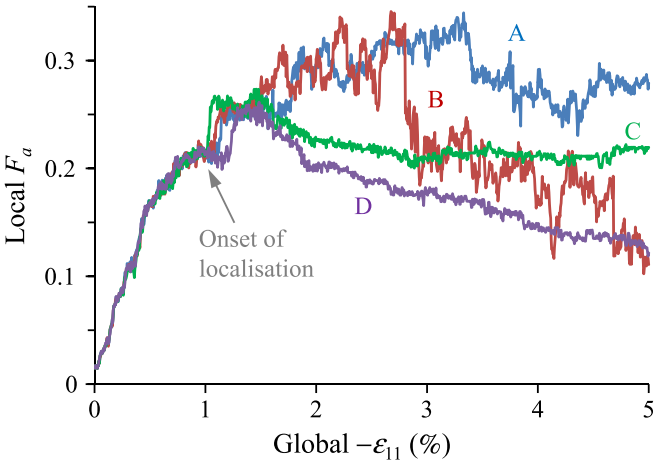

Fig. 19. Evolutions of fabric anisotropy of the selected local Gauss points of the dense specimen.

Meanwhile, the inherent feature of scale separation in the hierarchical multiscale framework also enables us to perform cross-scale analyses to seek microstructural insights into the macroscopic observations [13–17]. To quantify the microstructure of the material, we adopt the widely used contact normal-based fabric tensor following Ref. [57] (in 2D)

$$\phi_{ij} = \int_{\Theta} E(\Theta)\, n_i^c\, n_j^c = \frac{1}{N_c} \sum_{N_c} n_i^c\, n_j^c \tag{37}$$

$$E(\Theta) = \frac{1}{2\pi}(1 + \phi'_{ij}\, n_i^c\, n_j^c) \tag{38}$$

$$\phi'_{ij} = 4\left(\phi_{ij} - \frac{1}{2}\delta_{ij}\right) \tag{39}$$

where Θ is the orientation of the contact normal; $E(\Theta)$ is the probability distribution function. A scalar F_a $(=\sqrt{\phi'_{ij}\,\phi'_{ji}/2})$, is used to measure the anisotropic intensity. Fig. 19 presents the evolutions of F_a for the four selected Gauss points. The fabric anisotropy gradually increases upon loading in an almost identical manner for all four points until the onset of localisation, after which there is a small but drastic jump in F_a for all points due to the volume dilation at this stage (see Fig. 17(d)). After $\varepsilon_{11} = -1.5\%$, F_a of point D decreases steadily due to unloading; while F_a at point C decreases slightly due to volume contraction before reaching a roughly constant value. After the incipient of localisation, F_a at both points A and B increases with fluctuations before a softening-like behaviour is found at around $\varepsilon_{11} = -3\%$ for point B and slightly later for point A. The reduction in F_a for point B in the softening is more substantial than for point A, since the shearing at point B is indeed more intensive. It is instructive to examine the microstructures of the four points at the final stage, in forms of their interparticle contact force-chains and the contact normal distributions. As shown in Fig. 20, The RVEs at points A and B are both significantly deformed and rotated, especially for point B which is subjected to most intense shear at the centre of the shear band. Points C and D undergo rather small deformations as the packings still possess a largely square shape close to their initial state. For all cases, strong force-chains are found with its major orientation roughly aligned in the vertical direction, which is further confirmed by their rose diagrams showing more contacts in the vertical direction. From the rose diagrams, it is also seen that point A has the largest fabric anisotropy; Point C has the second largest; and the anisotropies at points B and D are close with smaller intensity. These observations are indeed consistent with Fig. 19.

The local responses of the loose specimen are also examined in a similar manner. Since the deformation is relatively uniform (diffuse failure) in the loose specimen, we only choose one Gauss point located at the centre of the specimen (labelled as E, see Fig. 15(b)) for investigation. Its responses are presented in Fig. 21. They are generally very similar to the global responses of the specimen, showing largely a contracting behaviour. The mean effective stress decreases continuously according to the loading path. An abrupt decrease in both the deviatoric stress and the mean effective stress is found at the final stage of loading (Fig. 21(a) and (b)), and causes the computation to abort. From Fig. 21(c),

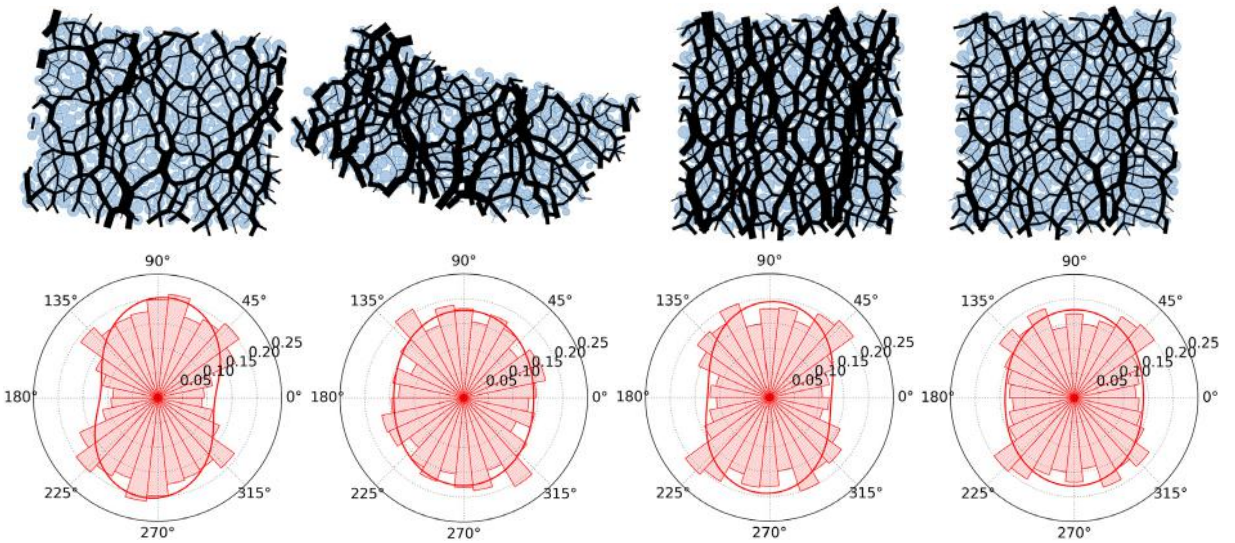

(a) Point A. (b) Point B. (c) Point C. (d) Point D.

Fig. 20. Force-chains and contact normal distributions of the selected local material points of the dense specimen at $\varepsilon_{11} = -5\%$.

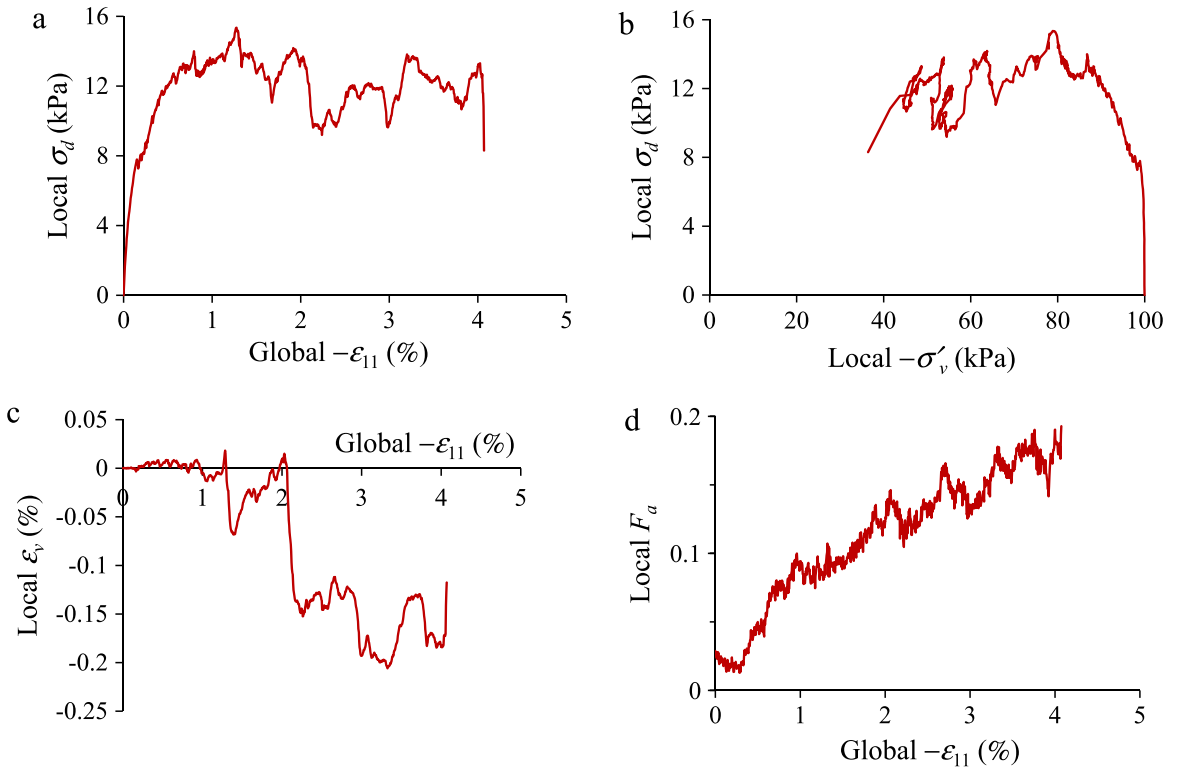

Fig. 21. Responses of the selected material point of the loose specimen: (a) evolutions of deviatoric stress; (b) loading path; (c) and (d) evolutions of volumetric strain and fabric anisotropy.

point E begins to experience volumetric contraction after $\varepsilon_{11} = -1\%$, resulting in the build-up of excess pore water pressure. The fabric anisotropy shown in Fig. 21(d) exhibits a general increasing trend. Notably, the responses of point E of the loose specimen are rather fluctuated, due probably to the small coordination number in the loose packing.

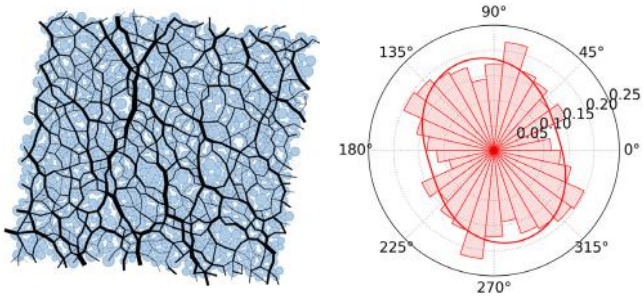

Fig. 22. Force-chain and contact normal distribution of the selected material point of the loose specimen at $\varepsilon_{11} = -4.05\%$ (prior to the final liquefaction state).

The microstructure of point E in terms of the force-chain and the contact normal distribution at $\varepsilon_{11} = -4.05\%$ (prior to the final liquefaction state) is shown in Fig. 22. The anisotropy is similar to those in the dense specimen, showing that more contacts are in the vertical direction. However, the force chains are significantly thinner (and hence indicatively smaller) than those of the dense specimen, since the stress level at point E is much lower than those Gauss points in the dense case at the final state. Indeed, the coordination number of point E at the final stage is only 2.8, indicative of a rather weak load–bearing, unstable structure, since a stable DEM packing with frictional particles normally requires a minimum coordination number of 3 in 2D [58]. As a result, with continuous shearing, the entire specimen enters liquefaction at $\varepsilon_{11} = -4.075\%$. For comparison, the selected four Gauss points of the dense specimen all have a coordination number greater than 3 at the final stage. Points A and B, which are inside the shear band and have undergone significant dilations, have a coordination number of 3.1 and 3.2, respectively. Points C and D, which only undergo small deformations, both have a coordination number of 3.6.

5. Conclusions

The original hierarchical multiscale approach [13–17] has been extended to model coupled hydro-mechanical problems for saturated granular soils. In the new framework, the governing equations of a fluid–solid system are solved based on the $\mathbf{u}$–p formulation [1], wherein the total stress is assumed to consist of the pore fluid pressure and the effective stress carried by the soil skeleton according to the Terzaghi's effective stress principle [24]. The effective stress is homogenised from the DEM solution of the RVE packing attached at each Gauss point of the FEM mesh to be used in the governing equations. A sequential iterative scheme based on the fixed-stress split method is employed to resolve the governing equations for the displacement and the pore pressure. The new formulation not only helps to bypass any need for conventional phenomenological constitutive assumptions, but well captures the complex behaviours of a saturated granular soil pertaining to its deformation, failure and pore fluid diffusion as well as fluid–soil interactions, which underpins a wide range of interesting phenomena in saturated soils such as strain localisation and liquefaction. Some key findings of the study are summarised below.

1. The fixed-stress split method [31–33] can be efficiently adapted for the hierarchical multiscale approach to solve the coupled $\mathbf{u}$–p equations for saturated granular soils. With only one extra term accounting for the pore fluid pressure added in the residual force, the original hierarchical multiscale formulation has been directly used as the mechanical solver in the fixed-stress split method. The independence of all local DEM computations enables a straightforward implementation of parallelisation for the approach, and the MPI-powered parallelisation shows a linear scalability of the code when being executed on an HPC cluster with single or multiple computing nodes.
2. The implemented coupled multiscale approach has been benchmarked by classical 1D and 2D consolidation problems on an elastic soil. The numerical predictions by the multiscale simulations compare fairly well with closed-form solutions of both the surface settlement and the pore fluid pressure dissipation [45,47] in the two problems.
3. Coupled multiscale simulations of globally undrained biaxial compression tests indicate that localised failure patterns with single shear band occur in dense specimen, and diffuse failure and liquefaction happen to the loose sample. The localisation in the dense specimen causes a softening response at large strain levels, while the loose specimen experiences a steadily contractive response. The fluid–soil interactions mark an interesting difference in

the two cases. In the dense specimen, the initiation of strain localisation is associated with a temporary water flux flowing from the other part of the specimen into the dilative shear band. When the shear band is fully developed, the water flow over the domain becomes negligible. Overall, the pore water pressure field is relatively uniform through the loading process. For the loose specimen, the contractive response gives rise to a rapid build-up of pore water pressure within the specimen, and hence a steady reduction of overall strength. Due to the deflection of the specimen, its corners experience relatively less volume contraction than its central area, leading to a flux pattern of water flowing from the central region into the two corners at the failure point.

4. Cross-scale analyses of the undrained biaxial compression results indicate microstructural differences in the dense and loose specimens. Material points inside the shear band of the dense specimen undergo rather significant volume dilations and softening responses, while the point outside the shear band experiences a small deformation followed by an unloading process. The material points located close to the edge of the shear band undergo pure volume contraction without shearing when the water flows out of these points into the shear band. All material points in the dense specimen possess an anisotropic structure, but those inside the shear band are more severely distorted. For the loose specimen, although having an anisotropic structure for its RVE packings, the force chains are much weaker than the dense case and the coordination number is below the minimum value required for a stable packing, which explains why the specimen loses its load-bearing capacity and enters liquefaction at the final state.

The study has been aimed for saturated granular soil. Nevertheless, as mentioned in the introduction, it remains possible to simulate unsaturated soil under the same framework, with further consideration of the capillary force in the RVE packing, e.g. by using the liquid-bridge model [28] to recover the *Bishop's effective stress* from the RVE packing. In addition to the quasi-static problems having been considered in the present study, the new framework may also be readily applied to treat dynamic or transient problems, e.g. when a soil is subjected to seismic loading or rainfall infiltration. In these cases, the influences of the pore water pressure and water flow are expected to be more significant. Indeed, in the transient/dynamic case, the Newmark scheme [1] may work well for the time integration and an explicit FEM could be used to solve for the acceleration of the soil solid. The explicit FEM used in [19,23] has been demonstrated being able to avoid the local Newton–Raphson iteration, and may also improve the overall efficiency of the coupled analysis. Furthermore, fundamental microscopic studies are still needed to establish a robust relationship between the microstructure of the RVE packing and the macroscopic permeability. The isotropic permeability assumed by the empirical Kozeny–Carman equation may differ considerably from the real case where an anisotropic permeability (a full permeability tensor) is more appropriate [59], especially when the microstructure of the RVE packing becomes highly anisotropic after external shearing as shown in Section 4.3. Worthy efforts should be made to address these aspects along the line of hierarchical multiscale modelling of granular media.

Acknowledgements

We acknowledge the Research Equipment Competition grants 2011–12 and 2013–14 at HKUST for acquiring the HPC cluster, the Research Grants Council of Hong Kong (GRF No. 623211) and a Theme-based Research Project (No. T22-603/15-N) for the financial support.

References

[1] O.C. Zienkiewicz, A.H.C. Chan, M. Pastor, B.A. Schrefler, T. Shiomi, Computational Geomechanics with Special Reference to Earthquake Engineering, John Wiley & Sons, Chichester, UK, 1999.
[2] J. Zhao, T. Shan, Coupled CFD–DEM simulation of fluid–particle interaction in geomechanics, Powder Technol. 239 (2013) 248–258.
[3] E. Catalano, B. Chareyre, E. Barthélémy, Pore-scale modeling of fluid-particles interaction and emerging poromechanical effects, Int. J. Numer. Anal. Methods Geomech. 38 (2014) 51–71.
[4] T. Shan, J. Zhao, A coupled CFD-DEM analysis of granular flow impacting on water reservoir, Acta Mech. 225 (2014) 2449–2470.
[5] Y.T. Feng, K. Han, D.R.J. Owen, Combined three-dimensional lattice Boltzmann method and discrete element method for modelling fluid–particle interactions with experimental assessment, Internat. J. Numer. Methods Engrg. 81 (2010) 229–245.
[6] D.R.J. Owen, C.R. Leonardi, Y.T. Feng, An efficient framework for fluid–structure interaction using the lattice Boltzmann method and immersed moving boundaries, Internat. J. Numer. Methods Engrg. 87 (2011) 66–95.
[7] Y. Han, P.A. Cundall, LBM–DEM modeling of fluid–solid interaction in porous media, Int. J. Numer. Anal. Methods Geomech. 37 (2013) 1391–1407.
[8] L. Hua, Stable element-free Galerkin solution procedures for the coupled soil–pore fluid problem, Internat. J. Numer. Methods Engrg. 86 (2011) 1000–1026.

[9] H.H. Bui, R. Fukagawa, An improved SPH method for saturated soils and its application to investigate the mechanisms of embankment failure: Case of hydrostatic pore-water pressure, Int. J. Numer. Anal. Methods Geomech. 37 (2013) 31–50.
[10] Y. Xie, G. Wang, A stabilized iterative scheme for coupled hydro-mechanical systems using reproducing kernel particle method, Internat. J. Numer. Methods Engrg. 99 (2014) 819–843.
[11] S. Bandara, K. Soga, Coupling of soil deformation and pore fluid flow using material point method, Comput. Geotech. 63 (2015) 199–214.
[12] M.A. Biot, General theory of three-dimensional consolidation, J. Appl. Phys. 12 (2) (1941) 155–164.
[13] N. Guo, J. Zhao, A hierarchical model for cross-scale simulation of granular media, in: AIP Conference Proceedings, Vol. 1542, 2013, pp. 1222–1225.
[14] N. Guo, J. Zhao, A coupled FEM/DEM approach for hierarchical multiscale modelling of granular media, Internat. J. Numer. Methods Engrg. 99 (11) (2014) 789–818.
[15] N. Guo, Multiscale characterization of the shear behavior of granular media (Ph.D. thesis), The Hong Kong University of Science and Technology, Hong Kong, 2014.
[16] J. Zhao, N. Guo, The interplay between anisotropy and strain localisation in granular soils: a multiscale insight, Géotechnique 65 (8) (2015) 642–656.
[17] N. Guo, J. Zhao, Multiscale insights into classical geomechanics problems, Int. J. Numer. Anal. Methods Geomech. 40 (3) (2016) 367–390.
[18] K. Kaneko, K. Terada, T. Kyoya, Y. Kishino, Global–local analysis of granular media in quasi-static equilibrium, Int. J. Solids Struct. 40 (2003) 4043–4069.
[19] C. Miehe, J. Dettmar, D. Zäh, Homogenization and two-scale simulations of granular materials for different microstructural constraints, Internat. J. Numer. Methods Engrg. 83 (2010) 1206–1236.
[20] J. Andrade, C. Avila, S. Hall, N. Lenoir, G. Viggiani, Multiscale modeling and characterization of granular matter: from grain kinematics to continuum mechanics, J. Mech. Phys. Solids 59 (2011) 237–250.
[21] T.K. Nguyen, G. Combe, D. Caillerie, J. Desrues, FEM × DEM modelling of cohesive granular materials: numerical homogenisation and multi-scale simulations, Acta Geophys. 62 (2014) 1109–1126.
[22] X. Li, Y. Liang, Q. Duan, B.A. Schrefler, Y. Du, A mixed finite element procedure of gradient Cosserat continuum for second-order computational homogenisation of granular materials, Comput. Mech. 54 (2014) 1331–1356.
[23] Y. Liu, W. Sun, Z. Yuan, J. Fish, A nonlocal multiscale discrete-continuum model for predicting mechanical behavior of granular materials, Internat. J. Numer. Methods Engrg. 106 (2) (2016) 129–160.
[24] K. Terzaghi, Principles of soil mechanics, Eng. News-Record 95 (1925) 19–27.
[25] J.A. White, R.I. Borja, Stabilized low-order finite elements for coupled solid-deformation/fluid-diffusion and their application to fault zone transients, Comput. Methods Appl. Mech. Engrg. 197 (2008) 4353–4366.
[26] W. Sun, J.T. Ostien, A.G. Salinger, A stabilized assumed deformation gradient finite element formulation for strongly coupled poromechanical simulations at finite strain, Int. J. Numer. Anal. Methods Geomech. 37 (2013) 2755–2788.
[27] X. Song, R.I. Borja, Mathematical framework for unsaturated flow in the finite deformation range, Internat. J. Numer. Methods Engrg. 97 (2014) 658–682.
[28] L. Scholtès, P.-Y. Hicher, F. Nicot, B. Chareyre, F. Darve, On the capillary stress tensor in wet granular materials, Int. J. Numer. Anal. Methods Geomech. 33 (2009) 1289–1313.
[29] W.K.S. Pao, R.W. Lewis, I. Masters, A fully coupled hydro-thermo-poro-mechanical model for black oil reservoir simulation, Int. J. Numer. Anal. Methods Geomech. 25 (2001) 1229–1256.
[30] M. Ferronato, N. Castelletto, G. Gambolati, A fully coupled 3-D mixed finite element model of Biot consolidation, J. Comput. Phys. 229 (2010) 4813–4830.
[31] J. Kim, H.A. Tchelepi, R. Juanes, Stability and convergence of sequential methods for coupled flow and geomechanics: Fixed-stress and fixed-strain splits, Comput. Methods Appl. Mech. Engrg. 200 (2011) 1591–1606.
[32] J. Kim, H.A. Tchelepi, R. Juanes, Stability and convergence of sequential methods for coupled flow and geomechanics: Drained and undrained splits, Comput. Methods Appl. Mech. Engrg. 200 (2011) 2094–2116.
[33] J. Kim, H.A. Tchelepi, R. Juanes, Stability, accuracy, and efficiency of sequential methods for coupled flow and geomechanics, SPE J. 16 (2) (2011) 249–262.
[34] P.C. Carman, Fluid flow through granular beds, Trans. Inst. Chem. Eng. 15 (1937) 150–166.
[35] J.E. Andrade, R.I. Borja, Modeling deformation banding in dense and loose fluid-saturated sands, Finite Elem. Anal. Des. 43 (2007) 361–383.
[36] L. Gross, L. Bourgouin, A.J. Hale, H.-B. Mühlhaus, Interface modeling in incompressible media using level sets in escript, Phys. Earth Planet. Inter. 163 (2007) 23–34.
[37] F. Brezzi, K.-J. Bathe, A discourse on the stability conditions for mixed finite element formulations, Comput. Methods Appl. Mech. Engrg. 82 (1–3) (1990) 27–57.
[38] J.R. Wren, R.I. Borja, Micromechanics of granular media Part II: Overall tangential moduli and localization model for periodic assemblies of circular disks, Comput. Methods Appl. Mech. Engrg. 141 (1997) 221–246.
[39] N. Kruyt, L. Rothenburg, Statistical theories for the elastic moduli of two-dimensional assemblies of granular materials, Internat. J. Engrg. Sci. 36 (1998) 1127–1142.
[40] V. Šmilauer, et al., Using and programming, in: Yade Documentation, second ed., 2015, http://dx.doi.org/10.5281/zenodo.34043. The Yade Project.
[41] R. Asadi, B. Ataie-Ashtiani, C.T. Simmons, Finite volume coupling strategies for the solution of a Biot consolidation model, Comput. Geotech. 55 (2014) 494–505.
[42] L. Dalcín, R. Paz, M. Storti, J. D'Elía, MPI for Python: Performance improvements and MPI-2 extensions, J. Parallel Distrib. Comput. 68 (2008) 655–662.
[43] F. Oka, Y. Higo, S. Kimoto, Effect of dilatancy on the strain localization of water-saturated elasto-viscoplastic soil, Int. J. Solids Struct. 39 (2002) 3625–3647.

[44] Y. Higo, F. Oka, M. Jiang, Y. Fujita, Effects of transport of pore water and material heterogeneity on strain localization of fluid-saturated gradient-dependent viscoplastic geomaterial, Int. J. Numer. Anal. Methods Geomech. 29 (2005) 495–523.
[45] A. Verruijt, S. van Baars, Soil Mechanics, VSSD, Delft, Netherlands, 2007.
[46] C. Geuzaine, J.-F. Remacle, Gmsh: A 3-D finite element mesh generator with built-in pre- and post-processing facilities, Internat. J. Numer. Methods Engrg. 79 (2009) 1309–1331.
[47] R.E. Gibson, R.L. Schiffman, S.L. Pu, Plane strain and axially symmetric consolidation of a clay layer on a smooth impervious base, Quart. J. Mech. Appl. Math. 23 (1970) 505–520.
[48] J. Mandel, Consolidation des sols (étude mathématique), Géotechnique 3 (7) (1953) 287–299.
[49] C.W. Cryer, A comparison of the three-dimensional consolidation theories of Biot and Terzaghi, Quart. J. Mech. Appl. Math. 16 (4) (1963) 401–412.
[50] F. Collin, R. Chambon, R. Charlier, A finite element method for poro mechanical modelling of geotechnical problems using local second gradient models, Internat. J. Numer. Methods Engrg. 65 (2006) 1749–1772.
[51] Y. Sieffert, O. Buzzi, F. Collin, Numerical study of shear band instability and effect of cavitation on the response of a specimen under undrained biaxial loading, Int. J. Solids Struct. 51 (2014) 1686–1696.
[52] K.J. McManus, R.O. Davis, Dilation-induced pore fluid cavitation in sands, Géotechnique 47 (1) (1997) 173–177.
[53] M. Yoshimine, P.K. Robertson, C.E. Wride, Undrained shear strength of clean sands to trigger flow liquefaction: Reply, Can. Geotech. J. 38 (3) (2001) 654–657.
[54] X. Liu, A. Scarpas, J. Blaauwendraad, Numerical modelling of nonlinear response of soil. part 2: Strain localization investigation on sand, Int. J. Solids Struct. 42 (2005) 1883–1907.
[55] G. Servant, F. Darve, J. Desrues, I.O. Georgopoulos, Diffuse modes of failure in geomaterials, in: H. DiBenedetto, T. Doanh, H. Geoffroy, C. Sauzéat (Eds.), Deformation Characteristics of Geomaterials: Recent Investigations and Prospects, Taylor & Francis Group, London, 2005, pp. 181–200.
[56] H.D.V. Khoa, I.O. Georgopoulos, F. Darve, F. Laouafa, Diffuse failure in geomaterials: Experiments and modelling, Comput. Geotech. 33 (2006) 1–14.
[57] M. Satake, Fabric tensor in granular materials, in: IUTAM Symposium on Deformation and Failure of Granular Materials, A.A. Balkema, Delft, 1982, pp. 63–68.
[58] A. Mehta, Granular Physics, Cambridge University Press, Cambridge, UK, 2007.
[59] W. Sun, J.E. Andrade, J.W. Rudnicki, P. Eichhubl, Connecting microstructural attributes and permeability from 3D tomographic image of in situ shear-enhanced compaction bands using multiscale computations, Geophys. Res. Lett. 38 (10) (2011) L10302.